The Dissertation Committee for Yerlan Amanbek
certifies that this is the approved version of the following dissertation:

Modeling flow and transport in porous media using a Enhanced Velocity scheme

Committee:

_____
Mary F. Wheeler, Supervisor

_____
Todd Arbogast

_____
Matthew Balhoff

_____
Yen-Hsi Richard Tsai

_____
Tim Wildey

Modeling flow and transport in porous media using a Enhanced Velocity scheme

by

Yerlan Amanbek

Dissertation

Presented to the Faculty of the Graduate School of

The University of Texas at Austin

in Partial Fulfillment

of the Requirements

for the Degree of

Doctor of Philosophy

The University of Texas at Austin

August 2018

Acknowledgments

Modeling flow and transport in porous media using a Enhanced Velocity scheme

by

Yerlan Amanbek
The University of Texas at Austin, 2018

Supervisor: Mary F. Wheeler

abstract in process We propose an adaptive multiscale approach to improve the efficiency and the accuracy of numerical computations by combining numerical homogenization and domain decomposition methods. The proposed approach minimizes the use of fine scale property information associated with an advection and diffusion problem in subsurface porous media for time varying boundary conditions. A fine scale flow and transport problem is solved in a smaller subdomain defined by a transient region where spatial changes in concentration is large while solving a coarse scale problem in the remaining domain. Away from the transient region, effective macroscopic equations are solved using upscaled properties calculated by local numerical homogenization. A fine grid discretization is then used in the transient region and a coarse grid everywhere else results in a non-matching multi-block problem. We then use an Enhanced Velocity Mixed Finite Element Method (EVMFEM) as a domain decomposition approach to couple these coarse and fine subdomains citewheeler2002enhanced. To the authors' knowledge, this approach

has not been investigated either theoretically or computationally in the existing literature. A number of numerical tests are also presented for verifying and demonstrating the capability of the adaptive numerical homogenization approach in upscaling flow and transport in porous medium.

Table of Contents

Chapter 1

Model formulations

1.1 Governing equations of flow and transport

We begin by describing the flow and transport model formulation along with initial and boundary conditions. We consider a single phase, slightly compressible fluid in porous medium with a non-reactive tracer transport for simplicity. The phase mass conservation equation on a domain Ω is given by,

$$\frac{\partial}{\partial t}(\phi\rho) + \nabla \cdot (\rho\mathbf{u}) = q \qquad \text{in} \quad \Omega \times J \tag{1.1}$$

where $\Omega \in \mathbb{R}^d (d = 1, 2 \text{ or } 3)$, $J = (0, T]$, d is the number of spatial dimensions, q is the source/sink term, ϕ is the porosity, ρ is the phase density, and $\mathbf{u}$ is the phase velocity. The slightly compressible fluid density is defined as a function of pressure as follows,

$$\rho = \rho_{ref} e^{C_f(p - p_{ref})} \tag{1.2}$$

where, C_f is the fluid compressibility, and ρ_{ref} is the reference density at reference pressure p_{ref}. Using Taylor series expansion we obtain $\rho \approx \rho_{ref}(1 + C_f(p - p_{ref}))$. Then it follows that $\phi\frac{\partial\rho}{\partial t} = \phi\frac{\partial\rho}{\partial p}\frac{\partial p}{\partial t} = \phi C_0 \frac{\partial p}{\partial t}$ for constant ϕ and for $C_0 = C_f\rho_{ref}$ with assumption $\rho \approx \rho_{ref}(1 + C_f(p - p_{ref}))$. The phase velocity $\mathbf{u}$ is given by the Darcy's law as,

$$\mathbf{u} = -\frac{\mathbf{K}}{\mu}\left(\nabla p - \rho\mathbf{g}\right), \tag{1.3}$$

where, μ is the viscosity, ρ is the phase density, $\mathbf{K}$ is the permeability (absolute permeability) tensor, and $\mathbf{g}$ is the gravity vector. Further, the conservation equation of a component i in the flowing phase is given by,

$$\frac{\partial}{\partial t}\left(\phi c_i \rho\right) + \nabla \cdot \left(c_i \rho \mathbf{u} - \phi \rho \mathbf{D}_i \nabla c_i\right) = q\hat{c}_i, \tag{1.4}$$

where, c_i and $\mathbf{D}_i$ is the normalized concentration and diffusion/dispersion tensor, respectively of component i in the flowing phase, and $\hat{c}_i$ is the injection/production concentration of the component i. We also define diffusive flux $\mathbf{d}_i$ for a component i as,

$$\mathbf{d}_i = \phi \mathbf{D}_i \nabla c_i, \tag{1.5}$$

for later use. The concentrations c_i are constrained by,

$$\sum_{i=1}^{N_c} c_i = 1. \tag{1.6}$$

General boundary conditions have been prescribed

$$p = g \quad \text{on} \quad \partial\Omega \times J \text{ , and}$$
$$\mathbf{D}_i \nabla c_i \cdot \nu = 0 \quad \text{on} \quad \partial\Omega \times J, \tag{1.7}$$

where ν is the unit outward normal;however, this is not restrictive and more general boundary conditions can be prescribed. Additionally, the initial condition is given by,

$$p(x,0) = p^0(x)$$
$$c_i(x,0) = c_i^0(x) \quad \text{at} \quad \Omega \times \{0\}. \tag{1.8}$$

Equations. 2.1 through 2.8 describe a well-posed problem for slightly compressible, single phase flow and transport in porous medium.

1.2 Enhanced Velocity Mixed FEM

Mixed Finite Element Method (MFEM) was initially introduced as a spatial discretization scheme by the engineering community [14, 20] in the late 70s for solving problems in solid continua. For flow in porous medium, the cell-centered finite difference scheme goes back to 50s and was later shown to be a mixed method in the early 80s by [29, 36]. Later works have applied this scheme for a wide range of applications in multicomponent, multiphase fluid flow [33, 11, 31] and transport in porous medium. The mixed scheme uses a high-order approximation for both pressure and velocity variables resulting in accurate fluxes and local mass conservation properties. Enhanced Velocity MFEM [37] and Multiscale Mortar Mixed Finite Element Method (MM MFEM) [9, 27, 10] are spatial domain decomposition approaches to handle non-matching, multi-block grids. MM MFEM has been used to accurately couples different flow physics in different subdomains through interface conditions; however, this results in an additional nested iteration loop for interface problems. The EVMFEM approach, on the other hand, is shown to have an order of magnitude faster performance, with similar accuracy, when compared to the mortar approach. Recently, a global Jacobian method for mortar discretization [17] of two-phase flow was developed that obtains similar computational efficiency compared to the original MM MFEM solution algorithm. Additionally, this approach is strongly mass conservative at the interfaces and strong continuity of fluxes between the subdomains.

EVMFEM has been applied successfully to a wide variety of complex

multicomponent, multiphase flow and transport processes in porous medium including equation of state (EOS), compositional flow [33]. Earlier implementations [37, 33] employed a solution approach where only the coarse and fine domain contributions to the stiffness-matrix (or Jacobian matrix) were taken, neglecting interface contributions. The load vector (or residuals); however, contains contributions from both the coarse and fine subdomains as well as the interface. This resulted in an increase in the number of non-linear iterations to achieve convergence, for a given tolerance, even for a linear flow and transport problem. In this work, we use a fully coupled variant of the original EVMFEM approach wherein the interface terms are properly accounted for in the stiffness-matrix construction resulting in reduced non-linear iterations (one for a linear system).

1.2.1 Governing equations of the incompressible flow

For convenience of analysis, we consider the incompressible single phase flow model for pressure p and the Darcy velocity $\mathbf{u}$:

$$\mathbf{u} = -\mathbf{K}\nabla p \qquad \text{in} \quad \Omega, \tag{1.9}$$

$$\nabla \cdot \mathbf{u} = f \qquad \text{in} \quad \Omega, \tag{1.10}$$

$$p = g \qquad \text{on} \quad \partial\Omega \tag{1.11}$$

where $\Omega \in \mathbb{R}^d (d = 2$ or $3)$ is multiblock domain, $f \in L^2(\Omega)$ and $\mathbf{K}$ is a symmetric, uniformly positive definite tensor representing the permeability divided by the viscosity with $L^\infty(\Omega)$ components, for some $0 < k_{min} < k_{max} <$

4

∞

$$k_{min}\xi^T\xi \leq \xi^T\mathbf{K}(x)\xi \leq k_{max}\xi^T\xi \qquad \forall x \in \Omega \quad \forall \xi \in \mathbb{R}^d. \qquad (1.12)$$

Let Ω be divided for series of small subdomains. The Dirichlet boundary condition considered merely for simplicity. We write this problem in mixed variational form, Sobolev spaces are exploited, the following space is defined for flux in $\mathbb{R}^d$ as usual to be

$$\mathbf{V} = H(\text{div}; \Omega) = \{\mathbf{v} \in \left(\text{L}^2(\Omega)\right)^\text{d} : \nabla \cdot \mathbf{v} \in \text{L}^2(\Omega)\}$$

and equipped with the norm

$$\|\mathbf{v}\|_V = \left(\|\mathbf{v}\|^2 + \|\nabla \cdot \mathbf{v}\|^2\right)^{\frac{1}{2}}$$

and for the pressure the space is

$$W = L^2(\Omega)$$

and the corresponding norm

$$\|w\|_W = \|w\|.$$

Our notations are made in usual manner. So for subdomain $\zeta \subset \mathbb{R}^d$, the $L^2(\zeta)$ inner product (or duality pairing) and norm are denoted by $(\cdot, \cdot)_S$ and $\|\cdot\|_\zeta$, respectively, for scalr and vector valued functions. Let $W^{m,p}$ be the standard Sobolev space of m-differentiable functions in $L^p(\zeta)$. Let $\|\cdot\|_{m,\zeta}$ be norm of $H^m(\zeta) = W^{m,2}(\zeta)$ or $H^m(\zeta)$, where ζ and m are omitted in case of

$\zeta = \Omega$ and $m = 0$ respectively, in other cases they are specified. We write $(\cdot, \cdot)$ for the $L^2(\zeta)$ or $(L^2(\zeta))^d$ inner product, and $\langle \cdot, \cdot \rangle_{\partial \zeta}$ for duality pairing on boundaries and interfaces, where the pairing may be between two functions in L^2 or between elements of $H^{1/2}$ and $H^{-1/2}$, in either order.

Next, a weak variational form of the fluid flow problem $(2.9) - (2.11)$ is to find a pair $\mathbf{u} \in \mathbf{V}$, $p \in W$

$$\left(\mathbf{K}^{-1}\mathbf{u}, \mathbf{v}\right) - (p, \nabla \cdot \mathbf{v}) = -\langle g, \mathbf{v} \cdot \nu \rangle_{\partial \Omega} \qquad \forall \mathbf{v} \in \mathbf{V} \qquad (1.13)$$

$$(\nabla \cdot \mathbf{u}, w) = (f, w) \qquad \forall w \in W \qquad (1.14)$$

where ν is the outward unit normal to $\partial \Omega$.
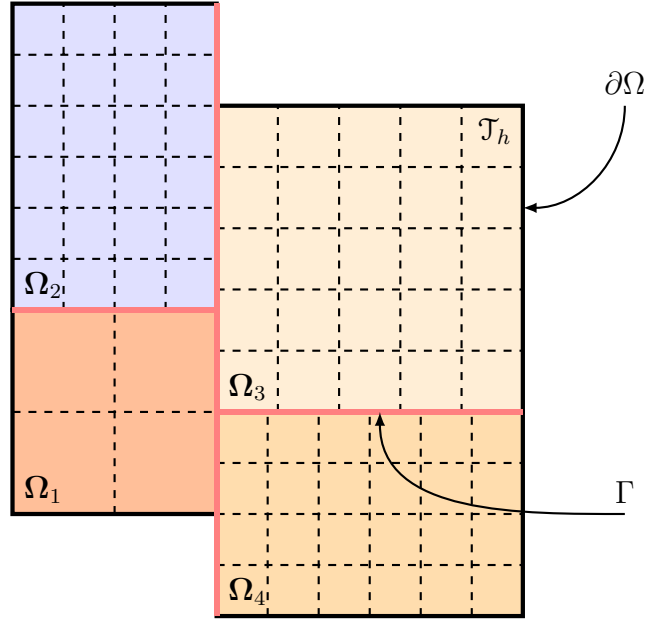
Figure 1.1: Illustration of a domain Ω with subdomains Ω_i and non-matching mesh $\mathcal{T}_h$.

6

Discrete formulation

We consider

$$\Omega = \bigcup_{i=1}^{N_b} \Omega_i \qquad \Gamma_{i,j} = \partial\Omega_i \bigcap \partial\Omega_j, \quad \Gamma = \bigcup_{i,j=1}^{N_b} \Gamma_{i,j}, \quad \Gamma_i = \Omega_i \bigcap \Gamma = \partial\Omega_j \setminus \partial\Omega.$$

This implies the domain is divided into N_b subdomains, the interface between i^{th} and j^{th} subdomains$(i \neq j)$, the interior subdomain interface for i^{th} subdomain and union of all such interfaces, respectively.

Let $\mathcal{T}_{h,i}$ be a conforming, rectangular partition of Ω_i, $1 \leq i \leq n$, with maximal element diameter h_i. We then set $\mathcal{T}_h = \cup_{i=1}^n \mathcal{T}_{h,i}$ and denote h the maximal element diameter in $\mathcal{T}_h$; note that $\mathcal{T}_h$ can be nonmatching as neighboring meshes $\mathcal{T}_{h,i}$ and $\mathcal{T}_{h,j}$ need not match on $\Gamma_{i,j}$.

We narrow our work to the regularly used Raviart-Thomas spaces of lowest order on rectangles for $d = 2$ and bricks for $d = 3$. The RT_0 spaces are defined for any element $T \in \mathcal{T}_h$ by the following spaces:

$$\mathbf{V}_h(T) = \{\mathbf{v} = (v_1, v_2) \text{ or } \mathbf{v} = (v_1, v_2, v_3) : v_l = \alpha_l + \beta_l x_l : \alpha_l, \beta_l \in \mathbb{R}; l = 1, ..d\} \quad \text{and}$$

$$W_h(T) = \{w = \text{constant}\}$$

For example, in case the element $T = [0, 1]^2$ we have the four velocities:

$$\mathbf{v}_L = \begin{pmatrix} 1 - x \\ 0 \end{pmatrix}, \qquad \mathbf{v}_R = \begin{pmatrix} x \\ 0 \end{pmatrix}, \qquad \mathbf{v}_B = \begin{pmatrix} 0 \\ 1 - y \end{pmatrix}, \qquad \mathbf{v}_T = \begin{pmatrix} 0 \\ y \end{pmatrix}.$$

In fact, a vector function in $\mathbf{V}_h$ can be determined uniquely by its normal components $\mathbf{v} \cdot \nu$ at midpoints of edges (in 2D) or face (in 3D) of T. This is illustrated in Figure 2.2. The degrees of freedom of $\mathbf{v} \in \mathbf{V}_h(T)$ was created by

7

these normal components. As shown in Figure 2.3, the degree of freedom for a pressure function $p \in W_h(T)$ is at center of T and piecewise constant inside of T.
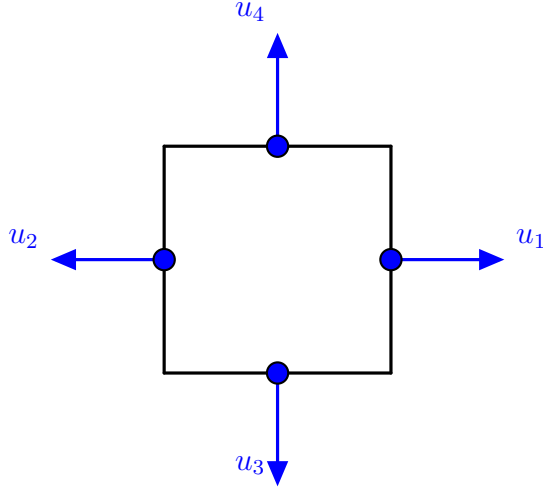
Figure 1.2: Degrees of freedom in the $RT_0(T)$ space
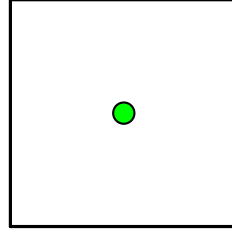
Figure 1.3: Degrees of freedom in the $P_0(T)$ space

The pressure finite element approximation space on Ω is taken to be in usual manner as

$$W_h(\Omega) = \{w \in L^2(\Omega) : w\Big|_E \in W_h(T), \forall T \in \mathcal{T}_h\}$$

We first construct a velocity finite element approximation space on Ω for velocity, which is different from the velocity space of the Multiscale Mortar Mixed FEM. Let us formulate RT_0 space on each subdomain Ω_i for partition $\mathcal{T}_h$

$$\mathbf{V}_{h,i} = \{\mathbf{v} \in H(\mathrm{div}; \Omega_i) : \mathbf{v}\Big|_T \in V_h(T), \forall T \in \mathcal{T}_{h,i}\} \qquad i \in \{1, ...n\}$$

8

and then

$$\mathbf{V}_h = \bigoplus_{i=1}^{n} \mathbf{V}_{h,i}.$$

Although the normal components of vectors in $\mathbf{V}_h$ are continuous between elements within each subdomains, the reader may see $\mathbf{V}_h$ is *not* a subspace of $H(\mathrm{div}; \Omega)$, because the normal components of the velocity vector may not match on subdomain interface Γ. To solve this issue, many researchers have proposed various methods such as Multiscale Mortar Mixed FEM [9], Enhanced Velocity Mixed FEM [37], etc. In Mortar Multiscale Mixed FEM , the mortar finite element space on coarse grid was introduced to connect subdomains together using Lagrange multipliers to enforce weak continuity for flux across subdomains. On the other hand, the Enhanced Velocity Mixed FEM modifies the degree of freedom on Γ to finer grids, which impose the strong flux continuity between subdomains. Let us define $\mathcal{T}_{h,i,j}$ as the intersection of the traces of $\mathcal{T}_{h,i}$ and $\mathcal{T}_{h,j}$, and let $\mathcal{T}_h^{\Gamma} = \bigcup_{1 \leq i \leq j \leq N_b} \mathcal{T}_{h,i,j}$. Fluxes are constructed to match on each element $e \in \mathcal{T}_h$. We consider any element $T \in \mathcal{T}_{h,i}$ that shares at least one edge with the interface Γ, i.e. $T \cap \Gamma_{i,j} \neq \emptyset$, where $1 \leq i, j \leq N_b$ and $i \neq j$. Then newly defined interface grid introduces a partition of the edge of T. This partition may be extended into the element T as shown in Figure 2.4.

This new partitioning helps to construct fine-scale fluxes that is in $H(\mathbf{div}, \Omega)$. So we represent a basis function $\mathbf{v}_{T_k}$ in the $\mathbf{V}_h(T_k)$ space (RT_0)

9
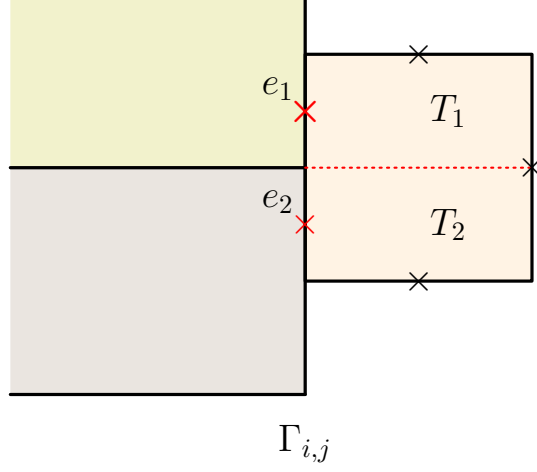
Figure 1.4: Degrees of freedom for the Enhanced Velocity space.

for given T_k with the following way:

$$\mathbf{v}_{T_k} \cdot \nu = \begin{cases} 1, & \text{on } e_k \\ 0, & \text{other edges} \end{cases}$$

i.e. a normal component $\mathbf{v}_{T_k} \cdot \nu$ equal to one on e_k and zero on all other edges(faces) of T_k. Let $\mathbf{V}_h^\Gamma$ be span of all such basis functions defined on all sub-elements induced the interface discretization $\mathcal{T}_{h,i,j}$. Thus, the enhanced velocity space $\mathbf{V}_h^*$ is taken to be as

$$\mathbf{V}_h^* = \bigoplus_{i=1}^{n} \mathbf{V}_{h,i}^0 \bigoplus \mathbf{V}_h^\Gamma \cap H(\operatorname{div}; \Omega).$$

where $\mathbf{V}_{h,i}^0 = \{\mathbf{v} \in \mathbf{V}_{h,i} : \mathbf{v} \cdot \nu = 0 \text{ on } \Gamma_i\}$ is the subspace of $\mathbf{V}_{h,i}$. The finer grid flux allows to velocity approximation on the interface and then form the $H(\operatorname{div}, \Omega)$ conforming velocity space. Some difficulties arise, however, in analysis of method and implementation of robust linear solver for such modification of RT_0 velocity space at all elements, which are adjoint to the interface

10

Γ. We now formulate the discrete variational form of equations $(2.9) - (2.11)$ as: Find $u_h \in \mathbf{V}_h^*$ and $p_h \in W_h$ such that

$$\left(K^{-1}\mathbf{u}_h, \mathbf{v}\right) = (p_h, \nabla \cdot \mathbf{v}) - \langle g, \mathbf{v} \cdot \nu \rangle_{\partial\Omega} \qquad \forall \mathbf{v} \in \mathbf{V}_h^* \qquad (1.15)$$

$$(\nabla \cdot \mathbf{u}_h, w) = (f, w) \qquad \forall w \in W_h \qquad (1.16)$$

1.2.2 Governing equations of the slightly compressible flow

We now consider the linear parabolic PDEs governing single phase flow model for pressure p and the velocity $\mathbf{u}$:

$$\mathbf{u} = -\mathbf{K}\nabla p \qquad \text{in} \quad \Omega \times J, \qquad (1.17)$$

$$\phi C_0 \frac{\partial p}{\partial t} + \nabla \cdot \mathbf{u} = f \qquad \text{in} \quad \Omega \times J, \qquad (1.18)$$

$$p = g \qquad \text{on} \quad \partial\Omega \times J, \qquad (1.19)$$

$$p = p_0 \qquad \text{in} \quad \Omega \times \{0\}. \qquad (1.20)$$

where $\Omega \in \mathbb{R}^d (d = 2 \text{ or } 3)$ is multiblock domain and $\mathbf{K}$ is a symmetric, uniformly positive definite tensor representing the permeability divided by the viscosity. The Dirichlet boundary condition is considered for convenience. We write the model in *semidiscrete* scheme that corresponds to the system where the solution is discretized in space, however, continuous in time. A weak solution of parabolic *Equations* (5.1)*to* (5.4) is a pair $\{\mathbf{u}, p\} : J \to H(\text{ div}; \Omega) \times L^2(\Omega)$

$$\left(K^{-1}\mathbf{u}, \mathbf{v}\right) - (p, \nabla \cdot \mathbf{v}) = -\langle g, \mathbf{v} \cdot \nu \rangle_{\partial\Omega} \qquad \forall \mathbf{v} \in \mathbf{V} \qquad (1.21)$$

$$\left(\phi C_0 \frac{\partial p}{\partial t}, w\right) + (\nabla \cdot \mathbf{u}, w) = (f, w) \qquad \forall w \in W \qquad (1.22)$$

11

In addition, there is an initial condition

$$(p, w)\Big|_{t=0} = (p_0, w) \qquad\qquad \forall w \in W \qquad (1.23)$$

We can now formulate the variational problem in discrete space as:

Find $\{\mathbf{u}_h, p_h\} : J \to \mathbf{V}_h^* \times W_h$ such that

$$\left(\mathbf{K}^{-1}\mathbf{u}_h, \mathbf{v}\right) - (p_h, \nabla \cdot \mathbf{v}) = -\langle g, \mathbf{v} \cdot \nu \rangle_{\partial\Omega} \qquad\qquad \forall \mathbf{v} \in \mathbf{V}_h^* \qquad (1.24)$$

$$\left(\phi C_0 \frac{\partial p_h}{\partial t}, w\right) + (\nabla \cdot \mathbf{u}_h, w) = (f, w) \qquad\qquad \forall w \in W_h \qquad (1.25)$$

with the weak initial condition $(p_h, w)\Big|_{t=0} = (p_0, w)$ for all $w \in W_h$.

Linear System

For simplicity , we show fully discrete form for the Backward Euler method in time : Find $\{\mathbf{u}_h, p_h\} : J \to \mathbf{V}_h^* \times W_h$ such that

$$\left(\mathbf{K}^{-1}\mathbf{u}_h^n, \mathbf{v}\right) - (p_h^n, \nabla \cdot \mathbf{v}) = -\langle g, \mathbf{v} \cdot \nu \rangle_{\partial\Omega} \qquad\qquad \forall \mathbf{v} \in \mathbf{V}_h^* \qquad (1.26)$$

$$\left(\phi C_0 \frac{p_h^n - p_h^{n-1}}{\Delta t}, w\right) + (\nabla \cdot \mathbf{u}_h^n, w) = (f^n, w) \qquad\qquad \forall w \in W_h \qquad (1.27)$$

where for any function Ψ we defined $\Psi^n = \Psi(x, t_n)$, $(0 \le n \le N)$. Later more general cases are written in Chapter 5 (a *priori* error analysis). We approximate the vector integrals type $(\mathbf{v}, \mathbf{q})_{T,M}$ by trapezoidal-midpoint quadrature rules and $(\mathbf{K}^{-1}\mathbf{q}, \mathbf{v})_T$ by trapezoidal quadrature rules respectively. In [29], the equivalence between finite volume methods and the mixed finite element method was established for special quadrature rule for $\mathbf{K}$ diagonal tensor and

using the lowest order Raviart Thomas spaces on rectangles. We emphasize that the EVMFEM with special quadrature and velocity elimination in the discrete system can be reduced to well-known a cell-centered finite difference method.

For each time step we use the Newton method to solve the system, because the fluid compressibility C_f term brings us to a nonlinear system and the consideration of it would be beneficial for nonlinear problems in the future. The discrete variational formulation yields a discrete system of form that was solved for each incremental terms of the Newton method as follows.

$$
\begin{bmatrix} A & -B \\ \Delta t B^T & D \end{bmatrix} \begin{bmatrix} \vec{\delta \mathbf{u}} \\ \vec{\delta \mathbf{p}} \end{bmatrix} = - \begin{bmatrix} \vec{G} \\ \vec{F} \end{bmatrix}. \tag{1.28}
$$

where $A_{i,j} = (\mathbf{K}^{-1}\mathbf{v}_i, \mathbf{v}_j)$, $B_{i,j} = (w_j, \nabla \cdot \mathbf{v}_i)$, $D_{i,j} = (\phi C_0 w_j, w_i)$, all these matrix blocks forms Jacobian matrix of partial derivatives, and $\vec{G}$, $\vec{F}$ correspond to residual equations of 2.24 and 2.25. We note that we drop the superscript in Equation 2.28.

We note that A is block diagonal matrix because inner product terms was computed a trapezoidal-midpoint quadrature rule in 2.26. Using EV scheme the velocity terms was replaced on the matrix system. This allows to modify the indefinite saddle point problem into only the pressure increment dependent system that is a non-symmetric positive definite. The increment value is necessary to update the next iteration values of pressure. To be spe-

cific, consider a Newton iteration number ν with an initial guess we have

$$\mathbf{J}^{n,\nu} \vec{\delta \mathbf{p}}^{\,n,\nu+1} = -\vec{\mathbf{R}}^{n,\nu}$$

$$\vec{\mathbf{p}}^{n,\nu+1} = \vec{\mathbf{p}}^{n,\nu} + \vec{\delta \mathbf{p}}^{\,n,\nu+1}$$

where $\mathbf{J}^{n,\nu} = \left(\Delta t B^T A^{-1} B - D\right)^{n,\nu}$ and $\vec{\mathbf{R}}^{n,\nu} = \left(\vec{F} - \Delta t B^T A^{-1} \vec{G}\right)^{n,\nu}$.

Chapter 2

Numerical homogenization method for single phase flow and transport

2.1 Introduction

Accurate modeling of flow and transport in subsurface is important in oil and gas recovery evaluations, nuclear waste disposal systems, CO_2 sequestration, and groundwater remediation in subsurface porous medium. Efficient numerical modeling of the associated physical processes has several challenges due to heterogeneity, uncertainty and multiscale nature of the porous media parameters. The main source of these parameters are usually borehole measurements which are sparsely distributed in space. The reservoir parameters are populated using these measurements in conjunction with geostatistical methods including parameter estimation and uncertainty quantification. However, a direct numerical simulation of the flow and transport problem, for a given scenario, using these fine scale parameters is often computationally prohibitive. Additionally, the datasets obtained from different observation sources vary strongly in characteristic spatial scales. For example, borehole and seismic measurements have a resolution varying between a few feet to hundreds of feet, respectively. A coarse scale numerical model, which can handle multiple Representative Elementary Volumes (REV), is therefore necessary to reduce computational overheads associated with solving a fine scale problem.

However, ad-hoc averaging techniques might fail to capture fine scale features resulting in loss of solution accuracy compromising the predictive nature of the model. Thus, development of mathematically consistent upscaling techniques is equally necessary for preserving solution accuracy at field scales. The multiscale nature of the flow and transport problems in porous medium has been addressed by several others [16, 6, 5, 8, 15, 38] giving rise to a number of approaches for upscaling. Each of these approaches performs computations at a coarse scale aiming to capture fine scale physics as closely as possible. However, one must note that all upscaling approaches tend to reduce fine scale property information either by averaging or by identifying reduced number of characteristic parameters. In what follows, we will discuss some of the key features of these approaches along with their shortcomings to the best of our understanding.

Homogenization theory is a well-established and mathematically consistent, theoretical framework for understanding multiscale nature of problems. Earlier studies by [3, 25, 22, 12, 4] to use homogenization theory for upscaling rapidly oscillating model parameters. For porous medium problems these parameters include rock properties such as permeability, porosity, dispersion as well as model parameters for relative permeability and heterogeneous chemical reactions. The two-scale homogenization theory relies upon the assumption of an identifiable period (or REV) in an otherwise heterogeneous medium with a characteristic length scale much smaller than the length scale of the medium under investigation. In other words, the ratio of the length of the period to

the medium, denoted by ε, is sufficiently small. This assumption leads to a scale separation between fine and coarse scale problems thereby decoupling the computations associated with each of these two problems. The effective properties at the coarse scale can then be evaluated given fine scale parameters following the two-scale homogenization theory in the limit of $\varepsilon \to 0$. Please note that this passing to the limit is a theoretical construct, for determining convergence, and in practice a small value of ε suffices. However, the requirements of periodicity and scale separation are often too restrictive for direct application to realistic, heterogenous, porous medium problems. Nevertheless, homogenization is an indispensable mathematical tool in providing insight into the multiscale nature of the problem by describing coarse scale parameters as functions of fine scale variations. In fact, homogenization theory has been used successfully to derive [24, 2] the constitutive law, well known as Darcy's law, for porous medium continua starting from Stoke's (Navier-Stokes) equation at the pore scale. A derivation of the model problem at hand using two-scale homogenization is discussed in Section 4.4. As we will show later, numerical homogenization used appropriately allows us to recover fine scale features with minimal loss in accuracy.

In this chapter, we investigate local numerical homogenization for upscaling permeability and porosity in heterogeneous porous media. We derive the effective parameters for slightly compressible case and we conduct numerical tests for the 10th SPE comparative project, which illustrates strong heterogeneity and complex structure that is typical in realistic problem of

17

subsurface flow.

2.2 Methodology

We use local numerical homogenization scheme inspired by two-scale homogenization theory to obtain effective equations at the coarse scale starting from fine scale mass conservation equation and constitutive relationship (Darcy's law).

2.2.1 Two-Scale Homogenization

The two-scale homogenization theory relies upon two major assumptions to derive effective equations at the field scale:

1. An identifiable periodic REV at a core scale of characteristic length l, with highly oscillatory (or heterogeneous) variations in parameters, in a macroscopic domain of another characteristic length scale L. These parameters include permeability, porosity as well as model parameters for heterogeneous chemical reactions.

2. A scale separation between the core and field scales such that the ratio between the two characteristic length scales, discussed above, is small $\varepsilon = l/L \to 0$.

As stated before, $\varepsilon \to 0$ is a theoretical requirement for two-scale homogenization and in practice a small value of ε is sufficient for accurate numerical computations. The scale separation assumption here inherently implies that the pressure, velocity and concentration unknowns vary slowly (relatively non-

18

oscillatory) at the field scale compared to faster variations (or highly oscilla-tory) at the core scale. Under the aforementioned two-scale ansatz the un-knowns in pressure, velocity, density and concentration are formally expanded as a power series in ε as,

$$a_\varepsilon(x) = a_0(x, y) + \varepsilon a_1(x, y) + \varepsilon^2 a_2(x, y) + ...$$

Here, a can be any one of the primary unknowns pressure (p), velocity $(\mathbf{u})$, density (ρ) or concentration (c). Further, x and y are the field and core scales such that $y = \frac{x}{\varepsilon}$ where $a(x, y)$ is used to denote the variations in an unknown at both the scales with periodic variations in $y \in Y$.

2.2.1.1 Flow

We begin by applying the two-scale homogenization theory to single phase slightly compressible flow problem in order to derive the effective flow equations at the coarse(field) scale. The parameters permeability and porosity are assumed to be oscillatory (or heterogeneous) parameters at the fine scale. The flow equations for slightly compressible flow at the fine scale have the following form

$$\mathbf{u}_\varepsilon = -\mathbf{K}\left(\frac{\mathbf{x}}{\varepsilon}\right)\nabla p_\varepsilon \qquad \text{in } \Omega$$

$$\frac{\partial}{\partial t}\left(\phi\left(\frac{\mathbf{x}}{\varepsilon}\right)\rho_\varepsilon\right) + \text{div}\left(\rho_\varepsilon\mathbf{u}_\varepsilon\right) = f \qquad \text{in } \Omega \tag{2.1}$$

$$p = g \qquad \text{on } \partial\Omega$$

where, ε denotes the two-scale variations in the unknowns $a_\varepsilon = a(x, y)$, $f \in L^2(\Omega)$ the source/sink term, and $\mathbf{K}$ and ϕ are the oscillatory (or heteroge-

19

neous) absolute permeability (symmetric, positive definite tensor) and porosity, respectively with period of oscillation $y = \frac{x}{\varepsilon}$, and $x, y \in \mathbb{R}^d$, $d = 1, 2, 3$. The two-scale gradient and divergence operators are then defined as,

$$\nabla = \nabla_x + \frac{1}{\varepsilon}\nabla_y \qquad \text{div} = \text{div}_x + \frac{1}{\varepsilon}\text{div}_y$$

Substituting, the formal expansion of the unknowns into the system of equations (3.1) we obtain,

$$\mathbf{u}_0 + \varepsilon\mathbf{u}_1 + \varepsilon^2\mathbf{u}_2 + ... = -\mathbf{K}\left(\nabla_x + \frac{1}{\varepsilon}\nabla_y\right)\left(p_0 + \varepsilon p_1 + \varepsilon^2 p_2 + ...\right)$$

$$\frac{\partial}{\partial t}\left(\phi\left(\rho_0 + \varepsilon\rho_1 + \varepsilon^2\rho_2 + ...\right)\right) \qquad (2.2)$$

$$+ \left(\text{div}_x + \frac{1}{\varepsilon}\text{div}_y\right)\left(\rho_0 + \varepsilon\rho_1 + \varepsilon^2\rho_2 + ...\right)\left(\mathbf{u}_0 + \varepsilon\mathbf{u}_1 + \varepsilon^2\mathbf{u}_2 + ...\right) = f$$

From the equations above, one can easily see that as $\varepsilon \to 0$, the unknowns $a_\varepsilon \to a_0$, or in other words the two scales are decoupled. Equating terms of like powers in ε in the above system provides us with effective equations at the coarse scale as follows,

1. For ε^{-1} terms:
$$-\mathbf{K}\nabla_y p_0 = 0$$

$$\text{div}_y\left(\rho_0\mathbf{u}_0\right) = 0$$

The solution to the above system is $p_0(x, y) = p_0(x)$ indicating that p_0 is only a function of coarse scale variations. In addition, we know that $\rho = \rho(p)$, or $\rho(p) = \rho_{ref}e^{C_f(p-p_{ref})} \approx \rho_{ref}\left(1 + C_f(p - p_{ref})\right)$, so

$$\rho_0 + \varepsilon\rho_1 + \varepsilon^2\rho_2 + ... \approx \rho_{ref}\left(1 + C_f(p_0 + \varepsilon p_1 + \varepsilon^2 p_2 + ... - p_{ref})\right)$$

20

By equating terms in power of ε, we note $\rho_0 = \rho_{ref}\left(1 + C_f(p_0(x,t) - p_{ref})\right)$.

It implies $\rho_0 = \rho_0(x,t)$, and then $\mathrm{div}_y(\mathbf{u}_0) = 0$.

2. For ε^0 terms:

$$u_0 = -\mathbf{K}\left(\nabla_x p_0 + \nabla_y p_1\right)$$

$$\frac{\partial}{\partial t}(\phi\rho_0) + \mathrm{div}_x(\rho_0\mathbf{u}_0) + \mathrm{div}_y(\rho_0\mathbf{u}_1 + \rho_1\mathbf{u}_0) = f$$

Since $\mathbf{u}_0$ is linear in p_0 and p_1, we can write $p_1(x,y,t)$ as,

$$p_1(x,y,t) = \sum_{i=1}^{3} \chi^i(y)\frac{\partial p_0}{\partial x_i}$$

In order to solve this system of equations we introduce an auxiliary problem, or a unit-cell problem for a dimensionless form of the above equations, on a periodic domain Y.

$$-\nabla \cdot \left(\mathbf{K}(y)\left(\nabla\chi^i + e_i\right)\right) = 0 \quad \text{in } Y$$

$$\chi^i \text{ is perodic in } Y \tag{2.3}$$

where $\{e_i\}_{1 \le i \le d} \in \mathbb{R}^d$ is the canonical basis for a finite dimensional problem of dimension d. Note that the solution vector χ^i is unique up to a constant. We obtain uniqueness by normalizing the non-unique solution with the mean of the solution such that $\int_Y \chi^i(y)dy = 0$.

3. The effective or homogenized equations at the coarse scale are then obtained by averaging the above system of equations over periodic domain

21

Y assuming $\varepsilon \to 0$.

$$\tilde{\mathbf{u}} = -\mathbf{K}^{eff} \nabla p_0 \qquad \text{in } \Omega$$

$$\frac{\partial}{\partial t} \left(\rho_0 \langle \phi \rangle \right) + \text{div}_{\text{x}} \left(\rho_0 \tilde{\mathbf{u}} \right) = f \qquad \text{in } \Omega \qquad (2.4)$$

$$p_0 = g \qquad \text{on } \partial\Omega$$

Here, $\tilde{\mathbf{u}} = \int_Y \mathbf{u}_0 dy$, $\langle \phi \rangle = \int_Y \phi dy$, $\mathbf{K}^{eff}$ is a symmetric, positive definite tensor denoting the effective permeability at the coarse scale. Note that the effective permeability does not depend on the choice of domain Ω, source term f, and boundary conditions on $\partial\Omega$. Further, the eigenvalues of the effective permeability tensor are bounded below and above harmonic and arithmetic means of eigenvalues of the fine scale permeability tensors. Arbogast [6] shows that the homogenized equations for the elliptic boundary value problem is well-posed which can be extended to the parabolic initial and boundary value problem discussed above. The effective permeability tensor is constructed using the solution (χ^i) of the auxiliary problem Eqn. (3.3) as follows,

$$\vec{w}^i(y) = -\mathbf{K}(y) \left(\nabla \chi^i + e_i \right) \text{ for } i = 1, .., d$$

$$Q(y) = [\vec{w}^1(y), \vec{w}^2(y), .., \vec{w}^d(y)]$$

$$\mathbf{K}^{eff} = -\langle Q \rangle = -\frac{1}{|Y|} \int_Y Q(y) dy$$
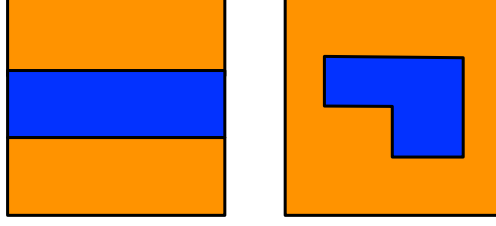
Figure 2.1: Schematic of REVs for layered (left) and general (right) permeability distribution.

An analytical derivation of effective permeability, using two-scale homogenization, for layered permeability distribution, with diagonal permeability tensor, is presented in [26]. It was confirmed theoretically and numerically in Appendix **??**. This results in the well-known arithmetic and harmonic averaging for flow along and across the layered medium, respectively. However, in order to use this result the REV must be chosen carefully so that the layered medium assumption and hence the aforementioned averaging applies. Figure 3.1 shows REV for layered and general distribution of permeability. One must note that it is not always possible to select an REV which satisfies the layered distribution wherein a more general approach such as numerical homogenization becomes indispensable. The numerical results section discusses the differences in results when the averaging approach for layered permeability REV is applied to a general heterogeneous case resulting in loss of connectivity of high perm channels.

2.2.1.2 Transport

A similar discourse as in the case of homogenizing flow equations above is applied to the advection/diffusion problem Eqn. 2.4 to obtain the effective equations at the macroscopic scale described below. Here we briefly discuss the derivation of these equations; following the original work for incompressible flow in [4], for the sake of completeness. Since $\rho_0 = \rho_0(x)$ or the ϵ^0 order density varies only at the coarse scale, the derivation of effective transport equations for slightly compressible flow remains unchanged from the original derivation for incompressible flow. We define $\varepsilon = l/L$, $Pe = u^0 l/D^0$, $t_c = \rho_0 \phi^0 L/u^0$ and denote u^0, D^0, K^0, ρ_0 and ϕ^0 as charateristic Darcy velocity, diffusivity, permeability and rock porosity respectively. Based on this setting we introduce dimensionless space variable $x \mapsto x/L$, the dimensionless characteristic convection time $t \mapsto t/t_c$ We keep assumptions including scale separation, $\varepsilon \ll 1$ and $Pe = O(1)$. In subsurface porous medium we observe a large diffusion at the coarse scale due to spreading, mixing and mechanical dispersion, and therefore Pe is assumed to be $O(1)$ so that convection does not dominate once derived macroscopic equations. The dimensionless form of the transport equation is given by,

$$\phi \left(\frac{x}{\varepsilon}\right) \frac{\partial (\rho_\varepsilon c_\varepsilon)}{\partial t} + \mathbf{u}^\varepsilon \cdot \nabla (\rho_\varepsilon c_\varepsilon) = \frac{\varepsilon}{Pe} \nabla \cdot \left(\rho_\varepsilon D \left(\frac{x}{\varepsilon}\right) \nabla c^\varepsilon \right) \qquad \text{on} \quad \Omega \times J,$$

$$c_\varepsilon(x,0) = c^0(x) \qquad\qquad \text{on} \quad \Omega \times \{0\}.$$

$$(2.5)$$

24

Using the two-scale ansatz,

$$c_\varepsilon(x) = c_0(x, y) + \varepsilon c_1(x, y) + \varepsilon^2 c_2(x, y) + ...,$$

$$\rho_\varepsilon(x) = \rho_0(x, y) + \varepsilon \rho_1(x, y) + \varepsilon^2 \rho_2(x, y) + ...,$$

$$\mathbf{u}_\varepsilon(x) = \mathbf{u}_0(x, y) + \varepsilon \mathbf{u}_1(x, y) + \varepsilon^2 \mathbf{u}_2(x, y) + ...$$

Substituting these expansions we obtain,

$$\phi \frac{\partial}{\partial t} \left((\rho_0 + \varepsilon \rho_1 + ...)(c_0 + \varepsilon c_1 + ...) \right)$$

$$+ (\mathbf{u}_0 + \varepsilon \mathbf{u}_1 + ...)(\nabla_x + \frac{1}{\varepsilon} \nabla_y)(\rho_0 + \varepsilon \rho_1 + ...)(c_0 + \varepsilon c_1 + ...)$$

$$= \frac{\varepsilon}{Pe} (\text{div}_x + \frac{1}{\varepsilon} \text{div}_y)(\rho_0 + \varepsilon \rho_1 + ...)D(\nabla_x + \frac{1}{\varepsilon} \nabla_y)(c_0 + \varepsilon c_1 + ...)$$

After collecting terms of the same ε-order one can obtain the following

1. For ε^{-1} terms:

$$\frac{1}{Pe} \text{div}_y(\rho_0 D \nabla_y c_0) - \mathbf{u}_0 \cdot \nabla_y (\rho_0 c_0) = 0$$

As before and $\rho_0 = \rho_0(x, t)$, this implies $c_0 = c_0(x, t)$.

2. For ε^0 terms we take into account that $c_0 = c_0(x, t)$:

$$\phi \frac{\partial(c_0 \rho_0)}{\partial t} + \mathbf{u}_0 \cdot \nabla_x(c_0 \rho_0) + \mathbf{u}_0 \cdot \nabla_y(c_1 \rho_0 + c_0 \rho_1) = \frac{\varepsilon}{Pe} \text{div}_y (\rho_0 D \nabla_x c_0) \quad (2.6)$$

Let us note that $\rho_0 = p_{ref} (1 + C_f(p_0(x, t) - p_{ref})) \approx \rho_{ref}$ due to $C_f <<$ 1. The homogenized equation, for ϵ^0 order accuracy in concentration, is obtained by integrating over the fine scale (Y),

$$\langle \phi \rangle \frac{\partial (\rho_0 c_0)}{\partial t} + \langle \mathbf{u}_0 \rangle \cdot \nabla_x (\rho_0 c_0) = 0, \quad (2.7)$$

25

where, $\langle w \rangle = \int\limits_{Y} w \, dy$

3. For ε^1 terms:

$$\phi \frac{\partial c_1}{\partial t} + \mathbf{u}_0 \cdot \nabla_y c_2 + \mathbf{u}_1 \cdot \nabla_x c_0 + \mathbf{u}_1 \cdot \nabla_y c_1$$

$$= \frac{1}{Pe} \left(\text{div}_x \left(D\nabla_x c_0 + D\nabla_y c_1 \right) + \text{div}_y \left(D\nabla_x c_1 + D\nabla_y c_2 \right) \right)$$

Similarly the homogenized equation; for ϵ^1 order accuracy in concentration, is given by,

$$\langle \phi \rangle \frac{\partial \left(\rho_\varepsilon^1 c_\varepsilon^1 \right)}{\partial t} + \langle \mathbf{u}_0 \rangle \cdot \nabla_x \left(\rho_\varepsilon^1 c_\varepsilon^1 \right) = \frac{\varepsilon}{Pe} \text{div}_x \left(\rho_\varepsilon^1 \mathbb{D}^{eff} \nabla_x c_\varepsilon^1 \right). \qquad (2.8)$$

Here, c_ε^1 and ρ_ε^1 are the coarse scale concentration and density respectively defined as $c_\varepsilon^1(x,t) = c_0 + \varepsilon c_1$, $\rho_\varepsilon^1(x,t) = \rho_0 + \varepsilon \rho_1$, it is

$$\rho_\varepsilon^1 c_\varepsilon^1 = \rho_0 c_0 + \varepsilon (\rho_0 c_1 + \rho_1 c_0) + O(\varepsilon^2) = \rho_0 c_0 + \varepsilon (\rho_0 c_1 + \rho_1 c_0).$$

We neglect the second-order terms. $\mathbb{D}^{eff}$ the effective diffusivity tensor, which is computed by solving auxiliary problem, $\langle \phi \rangle$ the volume averaged porosity, $\langle \mathbf{u}_0 \rangle$ the effective Darcy velocity, and Pe the Peclet number. First, we find the solution from the following problem: Find the periodic in Y solutions $\varphi_k(y; \vec{\lambda})$ of equations

$$-\text{div} \left(\mathbb{D}(y) \left(\nabla_y \varphi_k + \vec{e}_k \right) \right) + \mathbb{Q}(y) \vec{\lambda} \cdot \nabla_y \varphi_k = \left[\frac{\phi(y)}{\langle \phi \rangle} \langle \mathbb{Q} \rangle \vec{\lambda} - \mathbb{Q}(y) \vec{\lambda} \right] \cdot \vec{e}_k \quad \text{in } Y$$

$k = 1, ..d$, for every $\vec{\lambda} = Pe\nabla p_0(x)$. Second, we compute tensor

$$\mathcal{D}^h(\vec{\lambda}) \vec{e}_k = \langle \mathbb{D} \left(\nabla_y \varphi_k + \vec{e}_k \right) \rangle + \left\langle \left(\frac{\phi(y)}{\langle \phi \rangle} \langle \mathbb{Q} \rangle \vec{\lambda} - \mathbb{Q}(y) \vec{\lambda} \right) \varphi_k \right\rangle$$

26

Third, we evaluate

$$\mathcal{M}\left(\nabla p_0(x)\right)_{i,l} = \left(\mathbf{N}_{i,j}^2 \cdot \vec{e}_l\right) \partial_j p_0$$

where

$$\mathbf{N}_{i,j}^2 = \langle -\mathbf{K}\left(\nabla_y \chi_{i,j}^2 + \chi_i^1 e_j\right)\rangle$$

Then, we obtain the effective diffusivity for each $x \in \Omega$

$$\mathbb{D}^{eff}(x) = \mathcal{D}^h\left(Pe\nabla p_0(x)\right) + \mathcal{M}\left(Pe\nabla p_0(x)\right) \tag{2.9}$$

Here, for more details we refer the reader to [4].

2.2.2 Enhanced Velocity Mixed FEM Scheme

In this subsection, we briefly reiterate some parts of the derivation, presented in [33], for the multiblock, domain decomposition approach EVMFEM. This derivation is an extension of the original work for an incompressible, elliptic flow equation by [37] to a slightly compressible flow system. The model formulation has been described before in Section 2.2. We begin by describing the spaces for the velocity and pressure unknowns as,

$$\mathbf{V} = H(\text{div}; \Omega) = \{\mathbf{v} \in \left(L^2(\Omega)\right)^d : \nabla \cdot \mathbf{v} \in L^2(\Omega)\},$$

$$W = L^2(\Omega),$$

equipped with the following norms,

$$\|\mathbf{v}\|_V = \left(\|\mathbf{v}\|^2 + \|\nabla \cdot \mathbf{v}\|^2\right)^{\frac{1}{2}},$$

$$\|w\|_W = \|w\|.$$

A weak solution of the flow problem Eqns. 2.1-2.3 along with the boundary and initial condition in Eqns. 2.7-2.8, is the pair $\mathbf{u} \in L^2(J, V)$ and $p \in H^1(J, W)$ obtained by solving,

$$\left(\mathbf{K}^{-1}\mathbf{u}, \mathbf{v}\right) - (p, \nabla \cdot \mathbf{v}) = -\langle g, \mathbf{v} \cdot \nu \rangle_{\partial\Omega} \qquad \forall \mathbf{v} \in \mathbf{V}, \qquad (2.10)$$

$$\left(\phi C_f \rho_{ref} \frac{\partial p}{\partial t}, w\right) + (\nabla \cdot (\rho\mathbf{u}), w) = (f, w) \qquad \forall w \in W. \qquad (2.11)$$

Note here that $\mathbf{K}$ is a diagonal tensor. The initial condition

$$(p, w)\bigg|_{t=0} = (p_0, w) \qquad \forall w \in W \qquad (2.12)$$

Let denote $\Gamma_{i,j} = \partial\Omega_i \cap \partial\Omega_j$ denote the interface between subdomains Ω_i and Ω_j then $\Gamma = \cup_{i,j=1}^n \Gamma_{i,j}$ and $\Gamma_i = \Omega_i \cap \Gamma = \partial\Omega_i \backslash \partial\Omega$. The subdomain partitions, or the grid elements in each subdomain, $\mathcal{T}_{h,i}$ and $\mathcal{T}_{h,j}$ need not match on $\Gamma_{i,j}$ then, $\mathcal{T}_h = \cup_{i=1}^n \mathcal{T}_{h,i}$. We use the RT_0 and piecewise constant finite-element space for the velocity and pressure unknowns defined on an element $E \in \mathcal{T}_h$ as

$$V_h(E) = \{\mathbf{v} = (v_1, v_2) \text{ or } \mathbf{v} = (v_1, v_2, v_3) : v_l = \alpha_l + \beta_l x_l : \alpha_l, \beta_l \in \mathbb{R}; l = 1, ..d\},$$

and

$$W_h(\Omega) = \{w \in L^2(\Omega) : w\bigg|_E \in W_h(E), \forall E \in \mathcal{T}_h\}$$

, respectively. The EVMFEM scheme modifies the degrees of freedom on the interface Γ to accommodate the non-matching flux degrees of freedom from the adjacent blocks, as shown in Figure 3.2. Let $\tau_{h,i,j}$ be a rectangle partition

of $\Gamma_{i,j}$ obtained from intersection of the traces of $\mathcal{T}_{h,i}$ and $\mathcal{T}_{h,j}$. The enhanced velocity scheme forces the fluxes to match on each element edge $e \in \tau_{h,i,j}$.
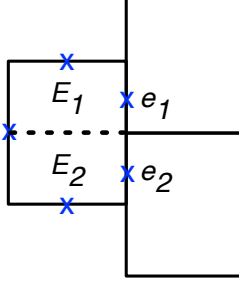

Figure 2.2: Degrees of freedom for the Enhanced Velocity Space.

On each sub-element E_k a basis function $\mathbf{v}_{E_k}$ is defined belonging to the RT_0 space $\mathbf{V}_h(E_k)$ as follows,

$$\mathbf{v}_{E_k} \cdot \nu = \begin{cases} 1 & \text{on } e_k, \\ 0 & \neq e_k. \end{cases}$$

Let $\mathbf{V}_h^\Gamma$ be span of all such basis functions. Then the multiblock mixed finite element velocity space is given by,

$$\mathbf{V}_h^* = \left(\mathbf{V}_{h,1}^0 \oplus \mathbf{V}_{h,2}^0 \oplus \cdots \oplus \mathbf{V}_{h,n}^0 \oplus \mathbf{V}_h^\Gamma\right) \cap H(\text{div}; \Omega).$$

Here, $\mathbf{V}_{h,i}^0$ is the subspace of $\mathbf{V}_{h,i}$ with zero normal trace on Γ_i. Also note that $\mathbf{V}_h^* \subset H(\mathbf{div}; \Omega)$. The variational problem in discrete space can then be written as: Find $\mathbf{u}_h \in L^2\left(J, \mathbf{V}_h^*\right)$ and $p_h \in H^1\left(J, W_h\right)$ such that,

$$\left(\mathbf{K}^{-1}\mathbf{u}_h, \mathbf{v}\right) - \left(p_h, \nabla \cdot \mathbf{v}_h\right) = -\langle g, \mathbf{v}_h \cdot \nu\rangle_{\partial\Omega} \qquad \forall \mathbf{v}_h \in \mathbf{V}_h^*,$$
$$(2.13)$$

$$\left(\phi C_f \rho_{ref} \frac{\partial p_h}{\partial t}, w_h\right) + \left(\nabla \cdot \left(\rho(p_h)\mathbf{u}_h\right), w_h\right) = \left(f, w_h\right) \qquad \forall w_h \in W_h.$$
$$(2.14)$$

The existence and uniqueness of this problem is shown in [37] for the elliptic case without applying the inf-sup condition directly. Here, error estimates were also derived for the problem at hand and a first order convergence was shown. We reiterated some of the earlier developments of EVM-FEM for single phase flow, next we extend this scheme for the transport or the advection/diffusion problem Eqn. (2.4), similar to [33]. Let us define $\mathbf{V}_h^{*,0} \equiv \mathbf{V}_h^* \cap \{\mathbf{v} : \mathbf{v} \cdot \nu = 0 \text{ on } \partial\Omega\}$ then the discrete variational problem; using the enhanced velocity space $\mathbf{V}_h^{*,0}$ for the diffusive/dispersive flux, is: Given $\mathbf{u}_h \in L^2(J, \mathbf{V}_h^*)$ and $p_h \in H^1(J, W_h)$, find $\mathbf{d}_{i,h} \in L^2\left(J, \mathbf{V}_h^{*,0}\right)$ and $c_{i,h} \in H^1(J, W_h)$ such that,

$$\left(\mathbf{D}_i^{-1}\mathbf{d}_{i,h}, \mathbf{v}_h\right) = (c_{i,h}, \nabla \cdot \mathbf{v}_h) \qquad \forall \mathbf{v}_h \in \mathbf{V}_h^{*,0}, \tag{2.15}$$

$$\left(\phi C_f \rho_{ref} \frac{\partial p_h}{\partial t} c_{i,h}, w_h\right) + \left(\phi\rho(p_h)\frac{\partial c_{i,h}}{\partial t}, w_h\right)$$

$$+ (\nabla \cdot (\rho(p_h)\mathbf{u}_h c_{i,h}), w_h) - (\nabla \cdot (\rho(p_h)\mathbf{d}_{i,h}), w_h) = (f, w_h) \qquad \forall w_h \in W_h.$$

In the above, we assume $\mathbf{D}_i > 0$. The EVMFEM ensures that both advective and diffusive fluxes are strongly continuous at the subdomain interfaces for this domain decomposition approach to be locally mass conservative. For single phase flow and tracer transport, the flow problem is inherently decoupled from the transport problem and therefore these two problems can be solved consecutively, as shown above. However, a fully coupled form can also be described as: Find $\mathbf{u}_h \in L^2(J, \mathbf{V}_h^*)$, $p_h \in H^1(J, W_h)$, $\mathbf{d}_{i,h} \in L^2\left(J, \mathbf{V}_h^{*,0}\right)$, and $c_{i,h} \in H^1(J, W_h)$ such that, Eqns. (3.13) thru (5.12) are satisfied.

30

2.2.3 Numerical Homogenization

We first perform numerical homogenization to obtain coarse scale parameters for a given set of fine scale properties. So we solve local auxiliary problem, Eqn. (3.3), using fine scale parameters on a set of subdomains with periodic boundary conditions to evaluate coarse scale parameters. The term local here is used to differentiate between numerical homogenization, for a globally periodic medium with a characteristic length scale, as opposed to a locally periodic or non-periodic medium. Figure 3.3 depicts global and local periodicities in porous medium. Please note that this figure is only for the purpose of illustration and the shapes of the microstructures chosen are of no consequence. These local periodicities are often observed in well log data where each layer represents a sedimentation and consolidation cycle.

Figure 2.3: Globally (left) and locally (right) periodic medium.

Figure 3.4 shows the horizontal permeability distribution for the Frio field pilot injection well obtained from well-logging [21] . The orange and blue zones identify the high and low permeability regions in the well log which allude to periodicity. Although, such an assumption is only valid for near

well-bore parameters (permeability, porosity etc.) characterized by a specific length scale. The periodicity assumption is often only valid for near well-bore parameters (permeability, porosity etc.) and can be characterized by a specific length scale. The periodic porous medium is a convenient construct for mathematical analysis; however, such an assumption is not always valid for realistic subsurface porous media problems. The reader is referred to [4] for further details regarding where a scale separation and periodicity is necessary for the theoretical framework or two-scale homogenization. In our work, we consider highly heterogeneous flow parameters where we relax these aforementioned assumptions.
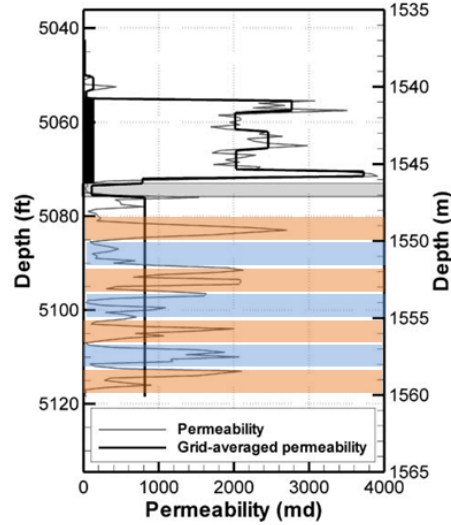
Figure 2.4: Horizontal permeability distribution with depth for Frio field injection well.

Figure 3.5 shows a schematic of this local numerical homogenization

where auxiliary problems are solved on a subdomain (Figure 3.5, Ω_i, dotted red, left) at the fine scale. Each of these cell problems provides a coarse scale parameter on the coarse grid (Figure 3.5, dotted red, right). These calculations are called offline since they are performed as a pre-processing step once prior to the actual numerical simulations. Subsection 3.3 in the numerical results section presents two examples where only numerical homogenization is used, without adaptivity, for both periodic and non-periodic media.
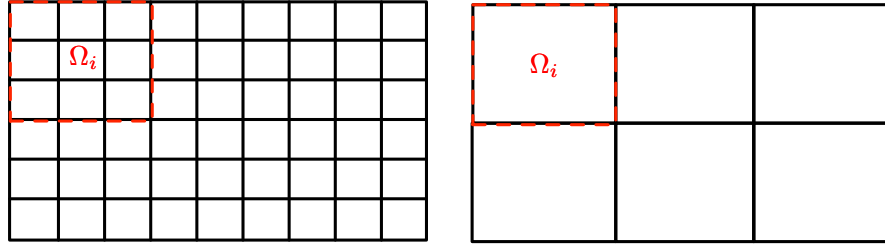
Figure 2.5: Schematic of numerical homogenization to obtain coarse scale (right) parameters from fine scale (left).

2.3   Numerical Results

In this section, we present two sets of numerical results for numerical homogenization. The tracer production curves are reported for each of the cases to demonstrate the effectiveness of the two approaches in capturing the fine scale flow and transport physics. The heterogenous porous medium is extracted from the 10th SPE comparative project for benchmarking different upscaling approaches. We report speedups by comparing coarse and fine scale simulation runtimes. One important point to note that the speedup factors

reported here takes into account the computational overheads due to the pre-processing or offline step.

We verify the numerical homogenization approach using a periodic medium followed by a local numerical homogenization on a highly heterogeneous (non-periodic) medium. The results are compared against fine scale simulations as the benchmark. The reservoir domain is 110ft $\times$ 30ft with fine scale permeability distribution available for a 220$\times$60 grid with grid block size 0.5ft$\times$0.5ft. A coarse scale permeability distribution for a 22$\times$6 grid is obtained by two-scale homogenization, as a preprocessing step at the beginning of the simulation, with grid block size of 5ft$\times$5ft. Here a local cell problem, for a 10$\times$10 grid, with periodic boundary conditions is solved at the fine scale. A rate specified injection well and pressure specified production well are located at the bottom left and top right corner, respectively. The production pressure is specified at 1000 psi with a continuous tracer injection at concentration 1. The initial reservoir pressure and concentrations are taken to be 1000 psi and zero (mass fraction), respectively with a fluid compressibility of 1×10^{-6} psi $^{-1}$. All simulations were performed for a total duration of 200 days with a no-flow external boundary condition unless explicitly stated otherwise in the subsections below. The timestep size is chosen to be 1 day for all the numerical experiments.

Verification of two-scale homogenization using periodic medium

We define a periodic medium where each period is characterized by a high permeability lens (yellow in Figure 3.1) $K_{xx} = 50mD$, $K_{yy} = 100mD$ in a low permeability porous matrix (blue in Figure 3.1) $K_{xx} = 5mD, K_{yy} = 10mD$. Figure 3.1 shows the global and local permeability distributions for the periodic medium and the unit cell, respectively. We took a small diffusion to be 0.001 in this case for simplicity. Further, a homogeneous reservoir porosity of 0.2 is considered with incompressible fluid description and an injection rate specification at 4 STB/day.
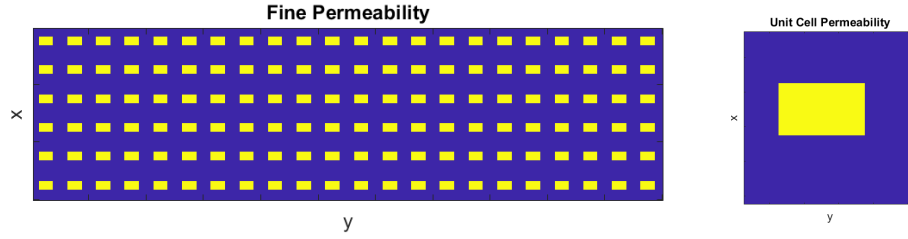
Figure 2.1: Global (left) and unit cell (right) permeability distributions.

Figure 3.2 shows the fine and coarse scale concentration profiles after 100 days of simulation run.
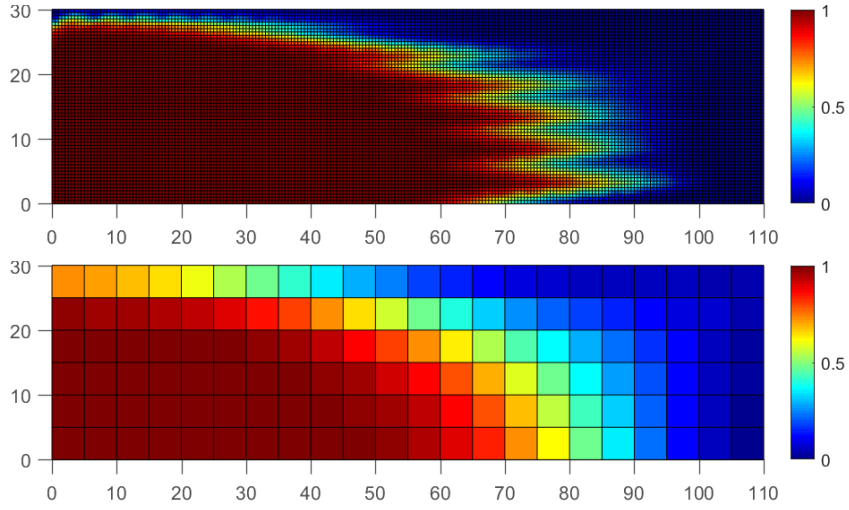
Figure 2.2: Concentration distributions for fine (top) and coarse (bottom) scale problems after 100 days.

Further, Figure 3.3 shows the tracer concentration history at the production well for the fine and coarse (or homogenized) cases. The fine and coarse scale results are in good agreement for this benchmark verification case. The coarse scale simulation run is approximately 400 times faster than the fine scale run which is attributed to the reduction in degrees of freedom (factor of 100) for the coarse scale simulation.
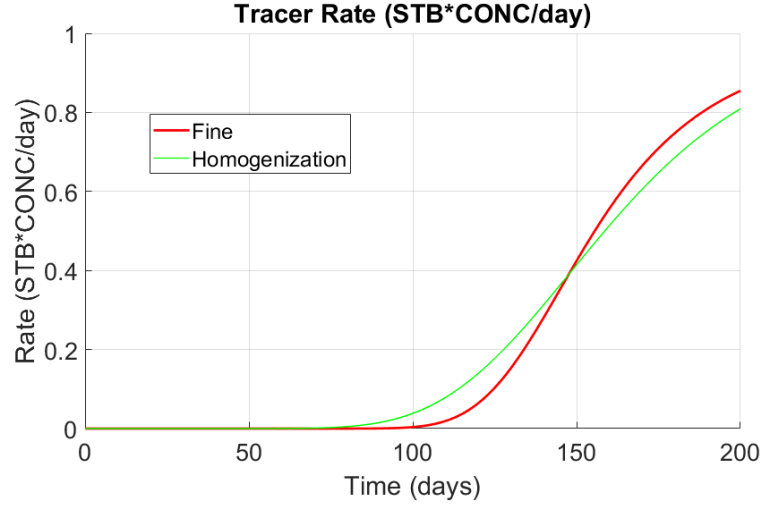
Figure 2.3: Tracer production history for fine and coarse (homogenized) scale problems.

Non-Periodic Medium

In this subsection, we consider a highly heterogeneous, non-periodic medium with respect to permeability and porosity distribution. We use the SPE10 comparative project for benchmarking upscaling approaches to obtain these distributions from layer 81 of the available dataset. Here, a channelized permeability distribution can be seen with high contrast in permeability values varying spatially over 6 orders in magnitude. Figure 3.5 shows one fine scale, from SPE10 layer 81, and two coarse scale permeability distributions obtained using local numerical homogenization and local harmonic-arithmetic averaging, respectively. A comparison is made against a local harmonic-arithmetic averaging commonly used by the engineering communities to upscale absolute permeability. The local harmonic-arithmetic averaging refers to harmonic av-

37

eraging in the direction of flow followed by arithmetic averaging orthogonal to the flow direction. Figure 3.4 shows a schematic of this approach to obtain effective (or upscaled) permeability in the horizontal direction. Please note that the coarse scale permeabilities obtained using local numerical homogenization preserve the channels, observed at the fine scale, as opposed to the harmonic averaging. Since numerically algorithm solving Equation 3.9 is computationally expensive at each time step and the clustering was proposed to compute for precomputed each λ in [4], we use a small diffusion coefficient number(1e-3), to achieve computational efficiency. The injection well is rate specified at 2 STB/day while keeping all other specifications unchanged.
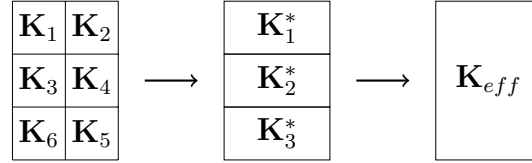
Figure 2.4: A harmonic-arithmetic averaging illustration
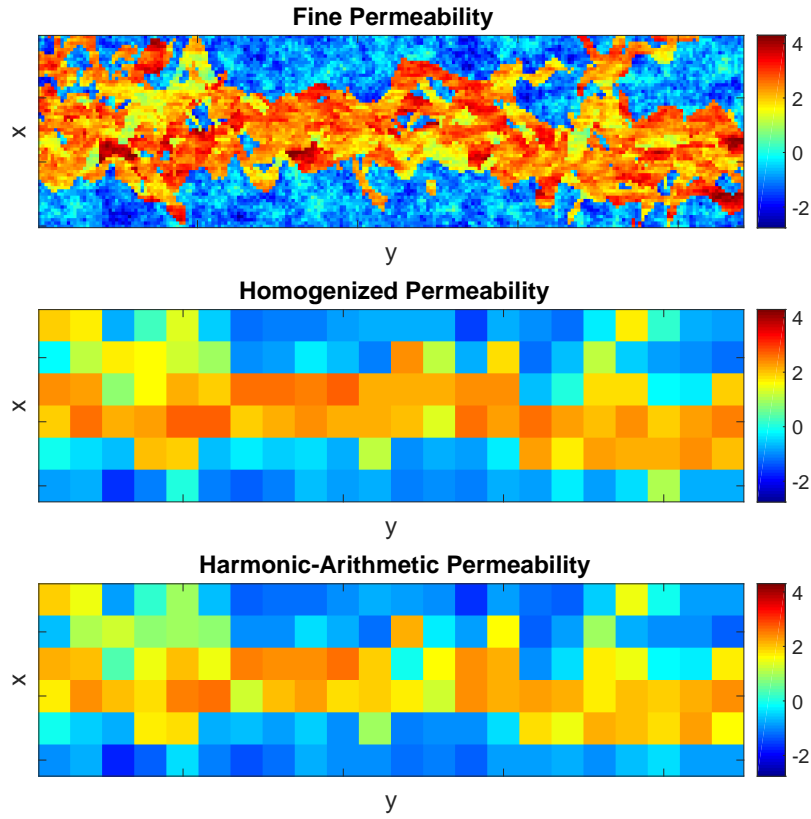
Figure 2.5: Permeability distributions for fine (top) and coarse harmonic (middle) and coarse homogenized (bottom) cases of SPE layer 81.

Figure 3.6 shows the concentration profiles for the three cases after 100 days of continuous tracer injection. As can be seen, the concentration profile for the harmonic-arithmetic average differs from the fine scale solution. This is clearly evident in the tracer concentration history, in Figure 3.7, where the harmonic average result deviates from the fine scale solution. Although, not a perfect match the numerical homogenization solution is closer to the fine scale solution even after a reduction in degrees of freedom from 26400 to 264 (factor

of 100). Computational speedups of approximately 400 times were observed for both local numerical homogenization and local harmonic-arithmetic averaging approaches when compared to the fine scale simulation.
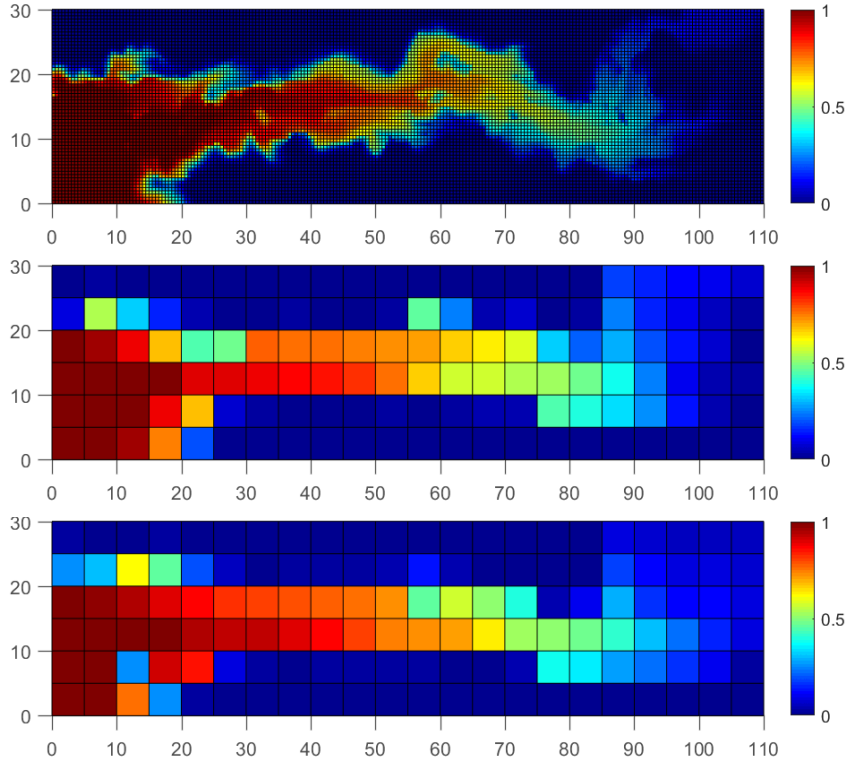
Figure 2.6: Concentration distributions for fine (top) and coarse homogenized (middle) and coarse harmonic-arithmetic (bottom) scales of SPE layer 81.
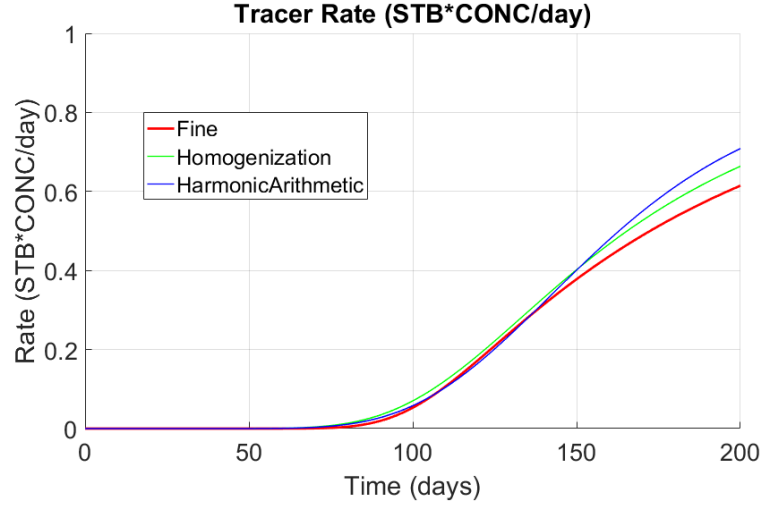
Figure 2.7: Tracer production history for fine and coarse (homogenized and harmonic-arithmetic average) scale problems.

2.4   Discussion

It is easily seen that the two concentration fronts would merge into one another due to this interconnectivity. Similar arguments can be extended for heterogeneous porous medium where differences in permeability and connectivity can result in mechanical mixing to different degrees. Moreover, the rapidly fluctuating velocity at fine scale may enforce to an enhanced dispersion, which can have discrepancy with dispersion resulting from macro scale setting. The challenge is to keep such connectivity pattern after the homogenization in macro scale setting for strong heterogeneous porous media. Next chapter, we can account for such phenomena using an Adaptive Mesh Refinement(AMR) approach to accurately capture the concentration front. This is necessary since homogenization approaches for advection and diffusion prob-

lem; although accurate, are computationally as expensive as solving the a local fine scale problem.

Chapter 3

Adaptive homogenization method using EVMFEM for single phase flow and transport

3.1 Introduction

In this chapter, we investigated local numerical homogenization for upscaling permeability and porosity. Furthermore, to obtain computational efficiency while maintaining solution accuracy at production well history we present an adaptive homogenization approach that combines this local numerical homogenization with Enhanced Velocity Mixed Finite Element Method (EVMFEM) [37] domain decomposition method. A fine scale problem is solved dynamically only in a subdomain coupled to a coarse problem solve in the rest of the domain. The fine subdomain is identified by sharp fronts associated with phase (or component) transport. In this aspect, our method shares similarities with the adaptive [13, 1] multiscale methods, where a coarse problem is enriched locally to capture fine scale physical features. We define transient region as subdomain in the visinity of these sharp fronts where spatial changes in concentration are significant. A fine spatial discretization is used in the transient region and everywhere else is a coarse discretization. Away from the transient region, effective macroscopic equations are solved at the coarse sclae with effective properties calculated using local numerical homogenization. This results in a non-matching multiblock problem which is then solved

using the EVMFEM which was developed by Wheeler et al. [37]. EVMFEM has been shown to be both reliable and accurate [33], and is an order of magnitude faster than the Multiscale Mortar Mixed Finite Element Method (MM MFEM).

3.2 Significants

Direct numerical simulations are often computationally prohibitive for practical subsurface applications. For accurately capturing fine scale features of heterogeneous porous media while remaining computationally efficient we propose a new adaptive numerical homogenization scheme using local numerical homogenization and the Enhanced Velocity Mixed Finite Element Method (EVMFEM) for single phase slightly compressible flow and transport. Our numerical results indicate a computational speedup of up to four times, compared to direct fine scale simulations, while preserving solution accuracy. The proposed adaptive numerical homogenization scheme for upscaling flow and transport in porous medium is in excellent agreement for Gaussian and layered distributions of porosity and permeability obtained from 10th SPE comparative project.

3.3 Highlights

- Local numerical homogenization for effective property evaluation combined with dynamic mesh refinement for computationally efficient and accurate representation of slightly compressible flow and transport physics.

44

- Verification, benchmarking and computational speedup reporting using datasets SPE 10th Comparative Project datasets. A practical metric for accuracy measurement is employed based upon a comparison of tracer concentration evolution with time at the production well.

- The approach can handle a wide range of property distributions such as permeability and porosity including Gaussian and layered (or channelized) distributions as shown in the numerical experiments.

- Adaptivity criterion can be altered to obtain breakeven between computational speedup and solution accuracy if required.

3.4 Methodology

In this work, we use local numerical homogenization scheme inspired by two-scale homogenization theory to obtain effective equations at the coarse scale starting from fine scale mass conservation equation and constitutive relationship (Darcy's law). Once the coefficients for the coarse scale equations have been evaluated, we use a domain decomposition approach to couple coarse and fine subdomains.

3.5 Adaptive Homogenization

The adaptive homogenization approach presented here has two key steps: (1) numerical homogenization to obtain parameters (permeability, porosity etc.) at the coarse scale by solving local auxiliary problems, (2) use EVM-FEM for AMR, with coarse and fine mesh regions identified using an adaptiv-

ity criterion, to solve coupled flow and transport problems. The subsections below describe the numerical homogenization and transient region identification using an indicator function. Here, a backward Euler scheme is used for temporal discretization resulting in a fully implicit system with spatial discretization using the fully-coupled, EVMFEM described in subsection 3.2.2. Since the solution scheme is fully implicit in pressure and concentration there is no time-step size restriction, as in the case of an explicit scheme where a CFL criteria is used. Further, an upwinding scheme is used for the advective flux term ($\mathbf{u}c_i$); to add sufficient diffusion, for the stability of the concentration solution.

3.5.1   Numerical Homogenization

We first perform numerical homogenization to obtain coarse scale parameters for a given set of fine scale properties. Here, we solve local auxiliary problem, Eqn. (3.3), using fine scale parameters on a set of subdomains with periodic boundary conditions to evaluate coarse scale parameters. The term local here is used to differentiate between numerical homogenization, for a globally periodic medium with a characteristic length scale, as opposed to a locally periodic or non-periodic medium. Figure 3.3 depicts global and local periodicities in porous medium. Please note that this figure is only for the purpose of illustration and the shapes of the microstructures chosen are of no consequence. These local periodicities are often observed in well log data where each layer represents a sedimentation and consolidation cycle. The pe-

riodicity assumption is often only valid for near well-bore parameters (permeability, porosity etc.) and can be characterized by a specific length scale. The periodic porous medium is a convenient construct for mathematical analysis; however, such an assumption is not always valid for realistic subsurface porous media problems. In our work, we consider highly heterogeneous flow parameters where we relax these aforementioned assumptions. Figure 3.5 shows a schematic of this local numerical homogenization where auxiliary problems are solved on a subdomain (Figure 3.5, Ω_i, dotted red, left) at the fine scale. Each of these cell problems provides a coarse scale parameter on the coarse grid (Figure 3.5, dotted red, right). These calculations are called offline since they are performed as a pre-processing step once prior to the actual numerical simulations. Subsection 3.3 in the numerical results section presents two examples where only numerical homogenization is used, without adaptivity, for both periodic and non-periodic media.

3.5.2   Transient Region Identification and Adaptivity Criteria

The adaptive homogenization approach, presented here, uses these coarse scale properties discussed above only in the non-transient region, identified by an indicator function. This indicator function (or adaptivity criterion) and details regarding transient/non-transient region demarcation are described here.

For multicomponent, flow and transport in porous medium the accuracy of the numerical solution depends upon how accurately the concentration front is captured. In order to capture the front accurately, the fluid velocities

47

must be resolved accurately along this concentration front since the component is transported by the fluid velocity. This necessitates that a fine scale problem be solved, with fine scale properties for flow and transport, in the vicinity of the front for accuracy. The computational overheads are reduced by solving a coarse scale problem away from the transient region using coarse scale properties obtained from numerical homogenization. We therefore define a transient region in space where the changes in concentration are larger than a given threshold. This notion has also been used earlier by others [1] to reduce computational costs associated with different problems. In this work, we use the following adaptivity criterion to identify the transient region for spatial domain decomposition:

$$\Omega_f = \{\mathbf{x} : \max|c^n(\mathbf{x}) - c^n(\mathbf{y})| > \epsilon_{adap} \quad \forall \mathbf{y} \in \Omega_{neighbor}(\mathbf{x})\} \qquad (3.1)$$

We define $\Omega_{neighbor}(\mathbf{x}) = \{\mathbf{y} : \mathbf{y} \in E_j, |\partial E_i \cap \partial E_j| \neq \emptyset, \text{if } \mathbf{x} \in E_i\}$. In other words, the criterion can be defined in space using a maximum of absolute of difference between a concentration c and its adjacent neighbors at the previous time step n.
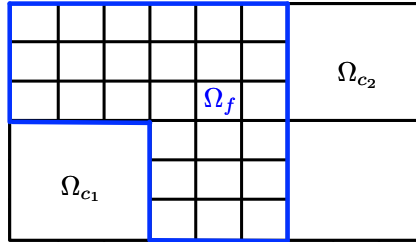
Figure 3.1: Schematic of adaptive mesh refinement with coarse (Ω_c) and fine (Ω_f) domains.

Based upon this criterion we divide the domain (Ω) into non-overlapping, transient (Ω_f) and non-transient (Ω_c) subdomains where flow and transport problems are solved at the fine and coarse scales, respectively. Figure 4.1 shows a schematic of the domain decomposition approach used here. In what follows, coarse and non-transient, and fine and transient can be used interchangeably to refer to a subdomain. Further, the coarse and fine subdomain problems are coupled at the interface using the EVMFEM spatial discretization described earlier in section 3.2.2.

3.5.3 Solution Algorithm

This subsection describes the solution algorithm for the adaptive homogenization approach discussed above. The local unit-cell (auxiliary) problems are solved as a pre-processing step to evaluate coarse scale coefficients using local numerical homogenization. This step can be carried out in parallel to further improve computational efficiency since the unit-cell problems are mutually independent. We refer to this calculation as the offline stage since the parameters (permeability, porosity, etc.) remain temporally invariant.

Algorithm 1 Adaptive multi-scale solution algorithm for the coupled flow and transport problem

---

Solve unit-cell problems, Eqns. (3.3), on subdomains (Ω_i) using fine scale parameters to obtain coarse scale parameters for the entire domain ($\Omega = \cup \Omega_i$, see Figure 3.3).

while $t_n \leq T$ **do**

    Identify transient (Ω_f) region using adaptivity criterion (Eqn. (4.1)) and p, c at t_n ($\Omega_f \cup \Omega_c = \Omega$).

    Mass conservative initialization of primary unknowns:

        1. Reconstruct primary unknowns $p^{n+1,0}, c^{n+1,0}$ for the fine scale transient region (Ω_f).

        2. Project primary unknowns $p^{n+1,0}, c^{n+1,0}$ for the coarse scale non-transient region (Ω_c).

    while $max(\vec{R}_{nl}) > \epsilon_{nl}$ **do**

        1. Use fine and coarse scale parameters in the transient (Ω_f) and non-transient (Ω_c) regions, respectively.

        2. Use enhanced velocity (EV) scheme to couple coarse and fine subdomains.

        3. Solve linear algebraic system for the coupled flow and transport problem to obtain a Newton update $p^{n+1,k+1}, c^{n+1,k+1}$.

    end

    $t_{n+1} = t_n + \Delta t, n := n + 1$

end

Algorithm 1 shows a brief outline of the solution algorithm. Here, n and

k are the time and non-linear iteration counter, t_n and t_{n+1} are the current and next time, Δt current time-step size, T the final time, $max(\vec{R}_{nl})$ the max norm of the non-linear residual vector, and ϵ_{nl} the non-linear tolerance. At each time iterate, we evaluate the adaptivity criterion (Eqn. (4.1)); at the coarse scale, to identify the transient region and perform a domain decomposition into fine (Ω_f) and coarse Ω_c subdomains. A projection/reconstruction operation is performed if the identifier changes from coarse to fine or vice versa, respectively. The reconstruction is performed by simply using previous time step unknowns and since these are intensive properties the operation remains mass conservative. On the other hand a mass conservative projection (L^2 projection) is used for coarsening which reduces to a simple arithmetic average of fine scale unknowns (p, c) for an incompressible flow problems. This is followed by a non-linear solve of the system of algebraic equations resulting from spatial and temporal discretization after domain decomposition. The non-linear iterations are performed until the max norm satisfies a desired tolerance corresponding to the error in phase and component mass conservation equations. Significant computational savings are obtained for time dependent problems since the effective values of porosity and permeability are only evaluated once for a given fine scale distribution.

3.6   Numerical Results

As mentioned in earlier, we avoid additional calculations due to changes in process parameters using a mass conservative, AMR based upon the fully

coupled enhanced velocity approach. This also helps us to generalize the adaptive homogenization approach towards making it process independent. In this section, we present two sets of numerical results for the adaptive homogenization with one verification case. The tracer production curves are reported for each of the cases to demonstrate the effectiveness of the two approaches in capturing the fine scale flow and transport physics. The heterogenous porous medium is extracted from the 10th SPE comparative project for benchmarking different upscaling approaches. We report speedups by comparing coarse and fine scale simulation runtimes. One important point to note that the speedup factors reported here takes into account the computational overheads due to the pre-processing or offline step.

The results are compared against fine scale simulations as the benchmark. The reservoir domain is 110ft $\times$ 30ft with fine scale permeability distribution available for a 220$\times$60 grid with grid block size 0.5ft$\times$0.5ft. A coarse scale permeability distribution for a 22$\times$6 grid is obtained by two-scale homogenization, as a preprocessing step at the beginning of the simulation, with grid block size of 5ft$\times$5ft. Here a local cell problem, for a 10$\times$10 grid, with periodic boundary conditions is solved at the fine scale. A rate specified injection well and pressure specified production well are located at the bottom left and top right corner, respectively. The production pressure is specified at 1000 psi with a continuous tracer injection at concentration 1. The initial reservoir pressure and concentrations are taken to be 1000 psi and zero (mass fraction), respectively with a fluid compressibility of 1×10^{-6} psi $^{-1}$. All simu-

lations were performed for a total duration of 200 days with a no-flow external boundary condition unless explicitly stated otherwise in the subsections below. The timestep size is chosen to be 1 day for all the numerical experiments.

3.6.1 Adaptive Numerical Homogenization

In this section, we compare numerical results for the fine scale and coarse scale using the adaptive homogenization and numerical homogenization approaches, respectively. We begin with by numerically verifying the AMR using a benchmark homogeneous case. We observed computational speedups of up to 4 times with the adaptive homogenization approach compared to direct fine solve for the numerical heterogeneous experiments described below. This ratio will be more substantial on large-scale models, since the computational complexity of adaptive methods depends linearly on the model size. Moreover, the speedup can be increased further by lowering the tolerance of the adaptivity criterion however, this also results in reduced solution accuracy. Thus an optimal tolerance exists which provides a breakeven between solution accuracy and computational speedup. We also outline a procedure for identifying this optimal tolerance for which calculations can be performed as a pre-processing step. In addition, a saving in computation time can be achieved by utilizing parallelization mechanisms with modern and accessible multi-core computing resources.

The reservoir domain, initial and boundary conditions, well placement and specifications are kept the same as in the previous subsection. Further,

a constant injection rate of 2 STB/day is chosen for the entire simulation run. The heterogeneous permeability distributions are obtained from different layers of the SPE10 comparative project dataset. Although, porosity distributions are not shown here the coarse scale SPE 10 porosities were obtained from fine scale distributions by applying a simple volume averaging, Eqn. (3.7). Although not restrictive, the diffusion coefficient is chosen to be 0.001 for this numerical experiment. In what follows we choose two permeability distributions from SPE10 dataset: (1) layer 20 and (2) layer 37 with injection and production specified at the bottom left and upper right corners. It is important to note here that the accuracy of the solution, compared to the benchmark fine scale solution, can be increased further by using a stricter criterion for adaptivity in all of the following results.

Verification: Homogeneous Case

A homogeneous, isotropic permeability distribution is assumed using a diagonal permeability tensor of 50 mD and porosity is assumed 0.1 to verify the adaptive solution against fine scale solution.

Figure 3.1: Concentration profiles at 50 days for coarse (top) , fine (middle) and adaptive (bottom) approaches in homogeneous permeability and porosity

Figure 4.2 shows the tracer concentration history at the production well after 200 days. The fine and adaptive results are in excellent agreement. Since the fine scale permeability distribution is homogeneous the homogenized or coarse scale distribution is also spatially invariant at 50mD. The disagreement between homogenized and fine results can be directly attributed to the numerical diffusion owing to the coarse grid.
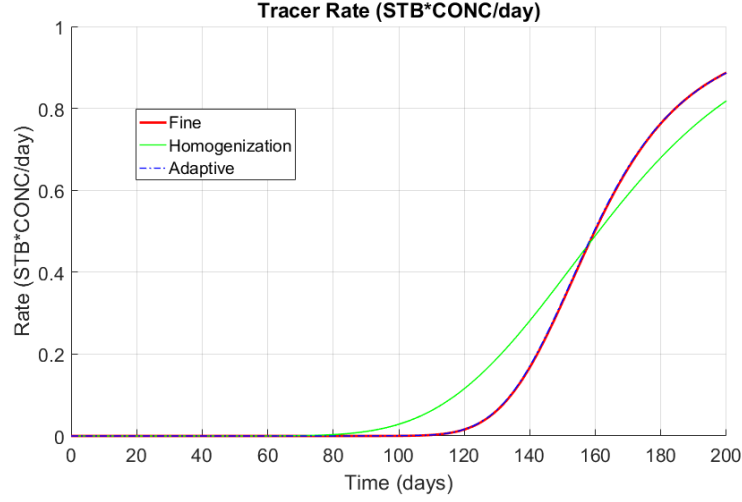
Figure 3.2: Tracer concentration history at production well for a homogeneous permeability distribution of 50 mD

Gaussian Permeability Distribution

For this numerical test, we choose the layered permeability distribution as shown in Fig. 4.3 (top) and the layered porosity obtained by extracting a slice of SPE10 dataset at layer 20. The coarse scale permeability, Fig. 4.3 (bottom), distribution and coarse scale porosity are evaluated using the numerical homogenization approach described before. This numerical test differs only in the injection rate, taken to be 3 STB/day, from all the other cases in what follows. Figure 4.5 shows the concentration profiles after 50 days for the coarse scale using homogenization, fine scale, and adaptive homogenization approaches. Figure 4.6 shows the tracer concentration history at the production well after 200 days. The results show that the concentrations using adaptive homogenization approaches are in good agreement with the fine scale solution.

56

Fine Permeability

Homogenized Permeability
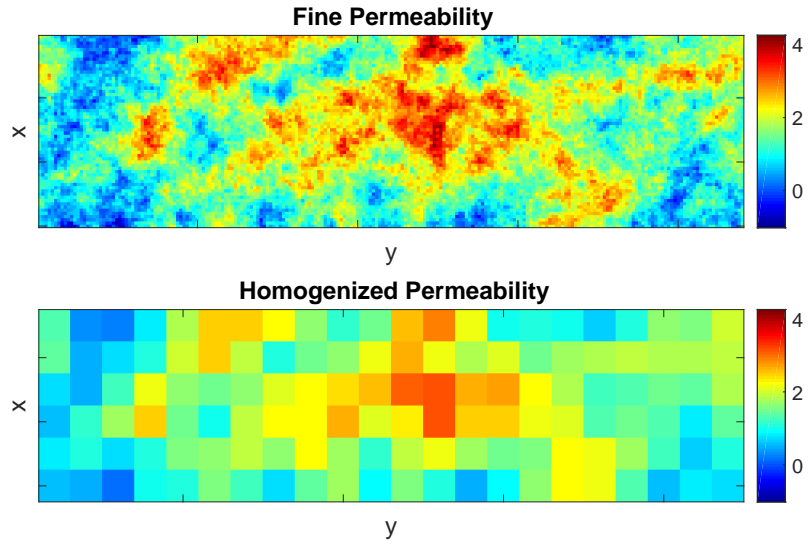
Figure 3.3: Fine and coarse scale permeability distributions in log scale for SPE 10 layer 20
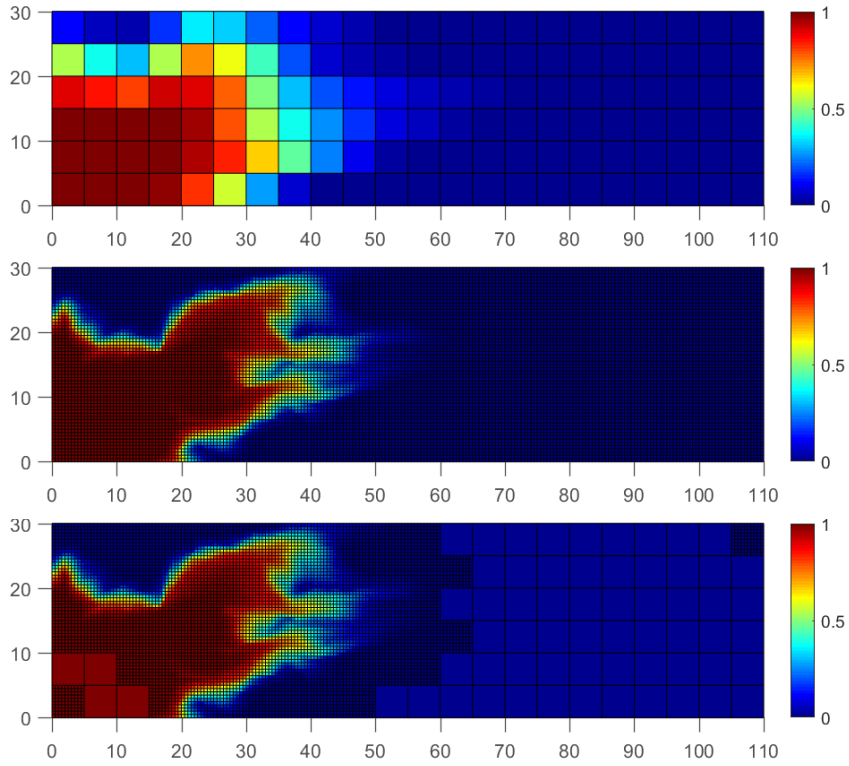
Figure 3.4: Concentration profiles at 50 days for coarse (top) , fine (middle) and adaptive (bottom) approaches   57
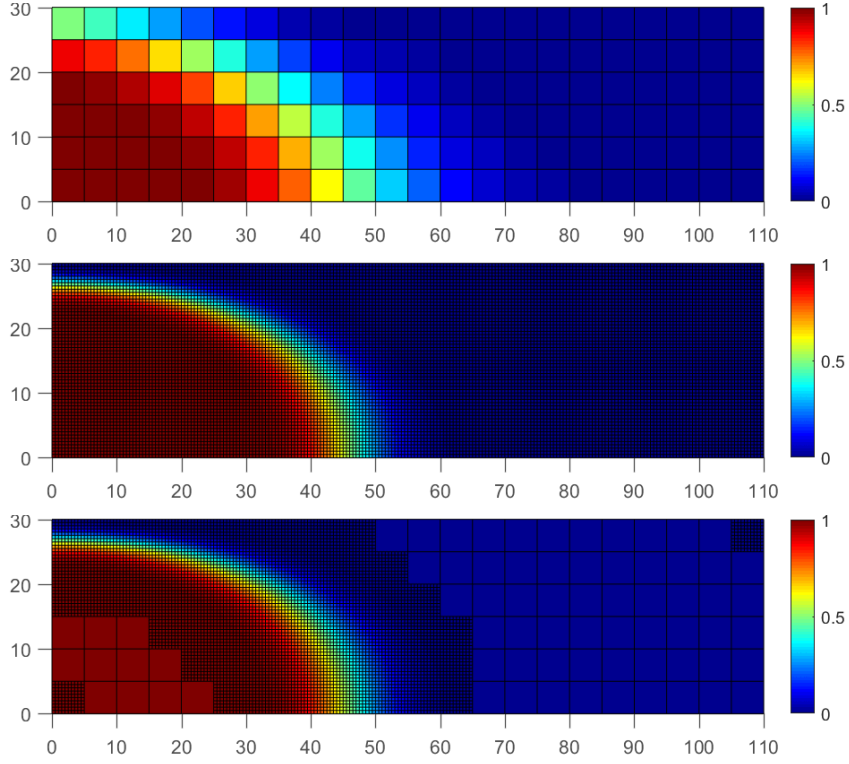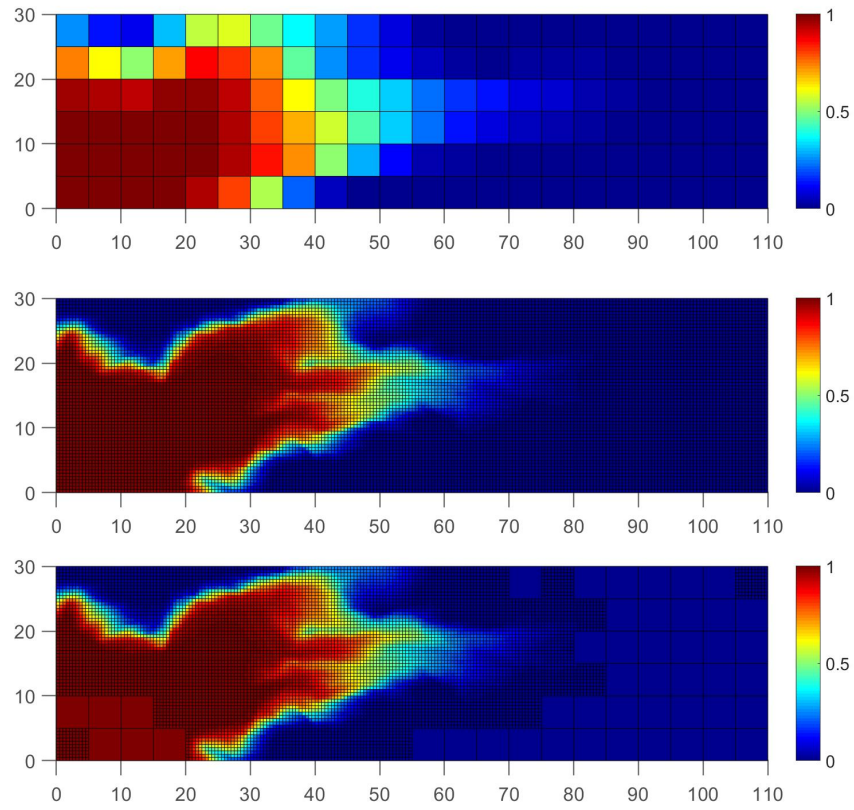
Figure 3.5: Concentration profiles at 70 days for coarse (top) , fine (middle) and adaptive (bottom) approaches
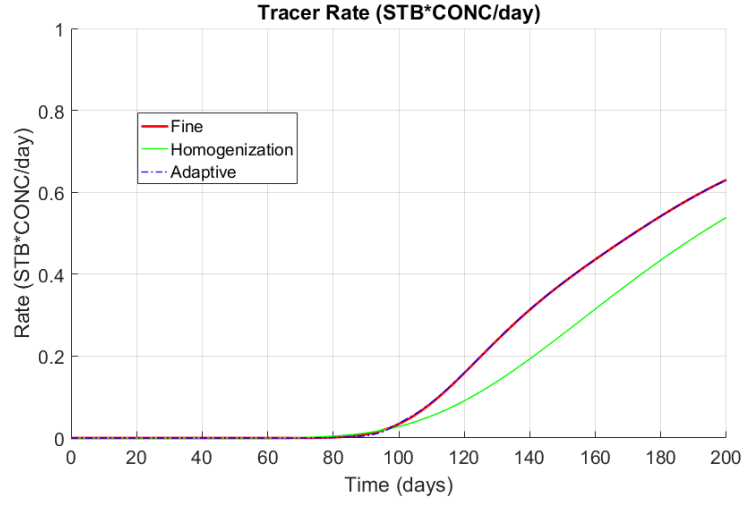
Figure 3.6: Tracer concentration history at the production well for SPE layer 20.

Channelized Permeability Distribution

Here we choose the permeability distribution from layer 37 of the SPE10 dataset. The coarse scale permeability distribution, Fig. 4.7 (bottom), distribution is evaluated as in the previous example.
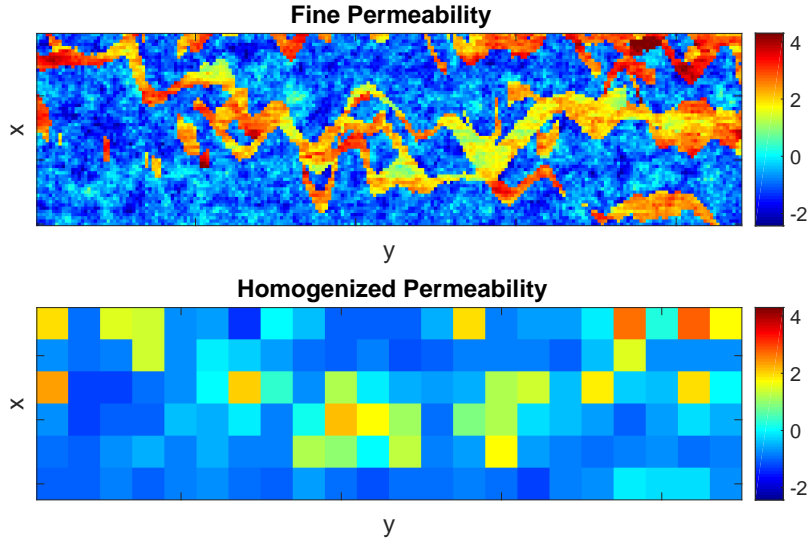
Figure 3.7: Fine and coarse scale permeability distributions in log scale for SPE 10 layer 37

Fig. 4.8 shows the concentration profiles after 50 days for the coarse scale using homogenization, fine scale, and adaptive homogenization approaches. These results indicated that even for highly channelized permeability distribution adaptive homogenization approach is able to accurately represent the concentration front when compared to the fine scale benchmark solution. In addition, in case inappropriate selection of REV the proposed approach captures concentration values at channels that efficiently leads to the accurate solution at the quantity of interest. The coarse scale using solely numerical homogenization however smudges the front substantially leading to drastic differences in breakthrough time prediction of the numerical simulation. Thus the adaptive homogenization approach is appropriate for both multimodal or layered permeability distributions in addition to Gaussian permeability distri-

butions.
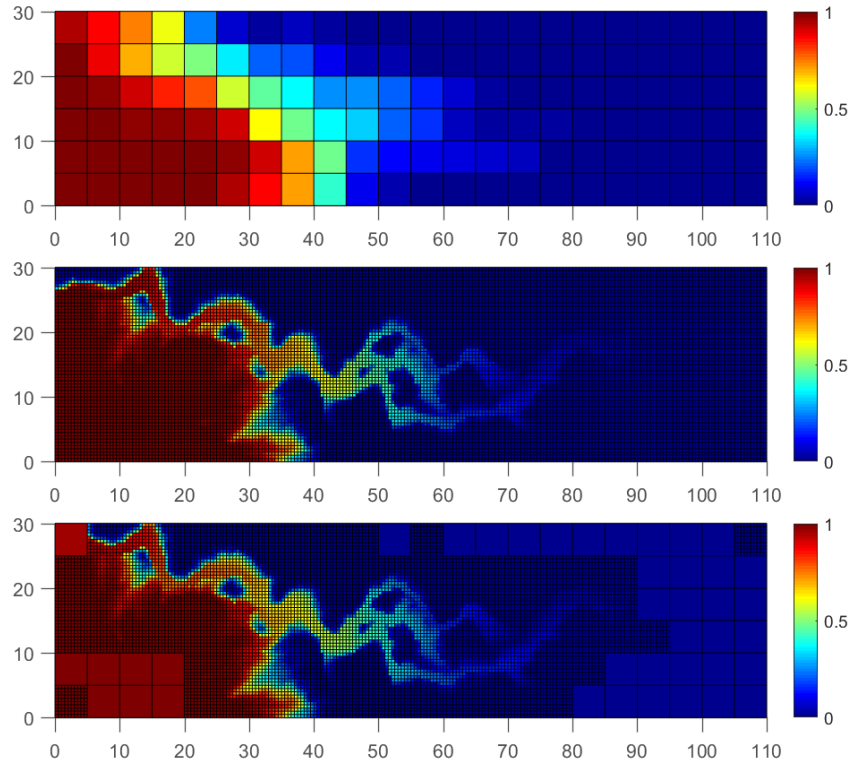
Figure 3.8: Concentration profiles at 50 days for coarse (top) , fine (middle) and adaptive (bottom) approaches
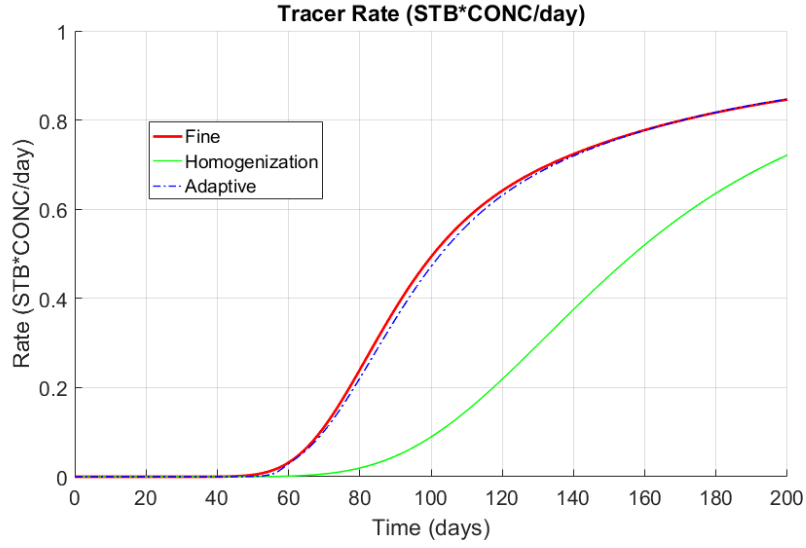
Figure 3.9: Tracer concentration history at the production well for SPE layer 37.

Figure 4.9 shows the tracer concentration history at the production well after 200 days. Please note that the homogenized, or coarse using numerical homogenization only, deviates more drastically from the fine scale solution for the layered permeability distribution (SPE layer 37) compared to the Gaussian permeability distribution (SPE layer 20) as shown in Figure 4.6.

Chapter 4

A *priori* error estimation for Parabolic problem with EVMFEM

4.1 Introduction

Many physical model including reservoir simulations, which are dynamic and time dependent problems, are important in the prediction of subsurface applications. This is often described by partial differential equations in integral forms and the solution can be approximated in the finite discretized domain. Numerical solution usually requires the procedure that maps from the continuum model into discrete or feasible space utilizing computational machine, which has several CPUs these days. The difference between analytical solution of the initial pde and the discrete space solution is can be taken as a numerical error. A great effort has been devoted to the study of the numerical error for various technique to be able to control, measure and predict effectively, because the computational power is keep improving. The knowledge of error behavior knowing true solution beforehand is called a *priori* error analysis, which provides an important information on bound of approximation. This produces information on asymptotic behavior of numerical error for given mesh size and other discretization parameters. In addition, the convergence of the numerical method and the guarantee of the method stability can be concluded from such analysis.

In this chapter, we aim to study a *priori* error convergence estimates of the parabolic equations with derivations in both a continuous-time and a discrete-time settings. We formulate a finite element procedure for numerically approximating the slightly compressible single phase flow model. The same being true for linear parabolic PDEs governing single phase flow. We use Backward Euler method in time and Enhanced Velocity Mixed FEM in space for non-matching multiblock grids. We first derive theoretical a *priori* error estimates in continuous in time setting.

4.2 A *priori* error estimation for Parabolic with Enhanced velocity Mixed FEM, the continuous in time case

We start by considering the linear parabolic PDEs governing single phase flow model for pressure p and the velocity $\mathbf{u}$:

$$\mathbf{u} = -\mathbf{K}\nabla p \qquad in \quad \Omega, \tag{4.1}$$

$$\frac{\partial p}{\partial t} + \nabla \cdot \mathbf{u} = f \qquad in \quad \Omega, \tag{4.2}$$

$$p = g \qquad on \quad \partial\Omega \tag{4.3}$$

$$p = p_0 \qquad at \quad t = 0 \tag{4.4}$$

where $\Omega \in \mathbb{R}^d (d = 2 \text{ or } 3)$ is multiblock domain and $\mathbf{K}$ is a symmetric, uniformly positive definite tensor representing the permeability divided by the viscosity. The Dirichlet boundary condition is considered for convenience. A

weak solution of parabolic *Equations* (5.1)*to* (5.4) is a pair $\mathbf{u} \in \mathbf{V}$, $p \in W$

$$\left(K^{-1}\mathbf{u}, \mathbf{v}\right) = (p, \nabla \cdot \mathbf{v}) - \langle g, \mathbf{v} \cdot \nu \rangle_{\partial\Omega} \qquad \forall \mathbf{v} \in \mathbf{V} \qquad (4.5)$$

$$\left(\frac{\partial p}{\partial t}, w\right) + (\nabla \cdot \mathbf{u}, w) = (f, w) \qquad \forall w \in W \qquad (4.6)$$

In addition, there is an initial condition

$$(p, w)\bigg|_{t=0} = (p_0, w) \qquad \forall w \in W \qquad (4.7)$$

The variational problem in discrete space: Find $\mathbf{u}_h \in \mathbf{V}_h^*$ and $p_h \in W_h$ such that

$$\left(K^{-1}\mathbf{u}_h, \mathbf{v}\right) = (p_h, \nabla \cdot \mathbf{v}) - \langle g, \mathbf{v} \cdot \nu \rangle_{\partial\Omega} \qquad \forall \mathbf{v} \in \mathbf{V}_h^* \qquad (4.8)$$

$$\left(\frac{\partial p_h}{\partial t}, w\right) + (\nabla \cdot \mathbf{u}_h, w) = (f, w) \qquad \forall w \in W_h \qquad (4.9)$$

In addition, there is an initial condition

$$(p_h, w)\bigg|_{t=0} = (p_0, w) \qquad \forall w \in W_h \qquad (4.10)$$

Let consider the differences: $5.5 - 5.8$, $5.6 - 5.9$

$$\left(\mathbf{K}^{-1}(\mathbf{u} - \mathbf{u}_h), \mathbf{v}\right) - (p - p_h, \nabla \cdot \mathbf{v}) = 0 \qquad \forall \mathbf{v} \in \mathbf{V}_h^* \qquad (4.11)$$

$$\left(\frac{\partial}{\partial t}(p - p_h), w\right) + (\nabla \cdot (\mathbf{u} - \mathbf{u}_h), w) = 0 \qquad \forall w \in W_h \qquad (4.12)$$

65

Useful norms

Let $J = [0, T]$, $T < \infty$, $J \subset [0, \infty)$; $\mathbf{u} : J \to H$; e.g. $H = L^2(\Omega)$;

We will consider the norm as follows.

$$\|\mathbf{u}\|_{L^p(J;H)} = \left[\int_J \|\mathbf{u}(\cdot, t)\|_H^p \, dt \right]^{\frac{1}{p}} \qquad \text{for} \quad 1 \le p < \infty.$$

$$\|\mathbf{u}\|_{L^\infty(J;H)} = \operatorname*{ess\,sup}_{t \in J} \|\mathbf{u}(t)\|_H \qquad \text{for} \quad p = \infty.$$

Projections

We shall write an projection and auxiliary error of pressure and velocity as follows.

$$E_p^I = p - \hat{p}$$

$$E_p^A = \hat{p} - p_h$$

$$E_\mathbf{u}^I = \mathbf{u} - \Pi^* \mathbf{u}$$

$$E_\mathbf{u}^A = \Pi^* \mathbf{u} - \mathbf{u}_h$$

Note $\mathbf{u} - \mathbf{u}_h = E_\mathbf{u}^I + E_\mathbf{u}^A$ and $p - p_h = E_p^I + E_p^A$.

$$(p - \hat{p}, w) = \left(E_p^I, w \right) = 0 \qquad \forall w \in W_h \tag{4.13}$$

For $\mathbf{u} \in H^1(\Omega)$

$$(\nabla \cdot (\Pi^* \mathbf{u} - \mathbf{u}), w) = \left(\nabla \cdot E_\mathbf{u}^I, w \right) = 0 \qquad \forall w \in W_h \tag{4.14}$$

Lemma 4.2.1.

$$\left(\frac{\partial}{\partial t} E_p^I, w \right) = 0 \qquad \forall w \in W_h \tag{4.15}$$

66
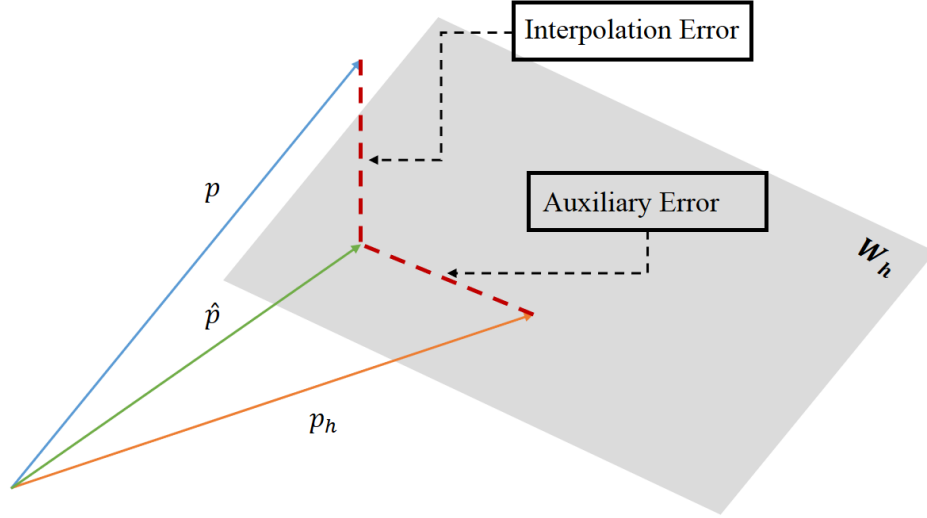
Figure 4.1: The time-dependent auxiliary and interpolation errors

Proof. $0 = \frac{d}{dt}\left(E_p^I, w\right) = \left(\frac{\partial}{\partial t}E_p^I, w\right) + \underbrace{\left(E_p^I, w_t\right)}_{0}$, by 5.13, since $w_t \in W_h$ □

Useful inequalities of projections , see [37]:

$$\left\|E_p^I\right\| \leq C \left\|p\right\|_r h^r \qquad 0 \leq r \leq 1 \tag{4.16}$$

$$\left\|E_{\mathbf{u}}^I\right\| \leq C \left\|\mathbf{u}\right\|_1 h \tag{4.17}$$

Recall Young's Inequality: for $a, b \geq 0$

$$ab \leq \frac{1}{2\varepsilon}a^2 + \frac{\varepsilon}{2}b^2 \tag{4.18}$$

The Inverse Inequality :

$$\left\|\nabla \cdot \mathbf{u}\right\| \leq Ch^{-1}\left\|\mathbf{u}\right\| \tag{4.19}$$

67

Theorem 4.2.2 (Auxiliary error estimate). *Let* 5.11 *and* 5.12. *For the velocity* $\mathbf{u_h}$ *and pressure* p_h *of the mixed method spaces* $\boldsymbol{V}_h^* \times W_h$ *we assume sufficient regularity for* $\mathbf{K}$*(symmetric, uniformly positive definite), there exist a constant* C *such that*

$$\left\| E_p^A \right\|_{L^\infty([0,T];L^2)}^2 + \left\| E_\mathbf{u}^A \right\|_{L^2([0,T];L^2)}^2 \leq C \left(h^2 \int_0^T \|\mathbf{u}\|_1^2 \, d\tau + h \int_0^T \|p\|_{1,\infty}^2 \, d\tau \right) \tag{4.20}$$

where $C=C(T,p,u,K)$.

Proof. Take $w = E_p^A$ in 5.12

$$\left(\frac{\partial}{\partial t}(p - p_h), E_p^A \right) + \left(\nabla \cdot (\mathbf{u} - \mathbf{u}_h), E_p^A \right) = 0$$

$$\left(\frac{\partial}{\partial t}(E_p^I + E_p^A), E_p^A \right) + \left(\nabla \cdot (E_\mathbf{u}^I + E_\mathbf{u}^A), E_p^A \right) = 0$$

$$\left(\underbrace{\frac{\partial}{\partial t}E_p^I, E_p^A}_{0 \text{ by } 5.15} \right) + \left(\frac{\partial}{\partial t}E_p^A, E_p^A \right) + \underbrace{\left(\nabla \cdot E_\mathbf{u}^I, E_p^A \right)}_{0 \text{ by } 5.14} + \left(\nabla \cdot E_\mathbf{u}^A, E_p^A \right) = 0$$

$$\left(\frac{\partial}{\partial t}E_p^A, E_p^A \right) + \left(\nabla \cdot E_\mathbf{u}^A, E_p^A \right) = 0$$

Note that $\left(\frac{\partial}{\partial t}E_p^A, E_p^A \right) = \frac{1}{2}\frac{d}{dt}\left\| E_p^A \right\|^2$. Therefore,

$$\frac{1}{2}\frac{d}{dt}\left\| E_p^A \right\|^2 + \left(\nabla \cdot E_\mathbf{u}^A, E_p^A \right) = 0 \tag{4.21}$$

68

Next, take $\mathbf{v} = E_{\mathbf{u}}^A$ in 5.11

$$\left(K^{-1}(\mathbf{u} - \mathbf{u}_h), E_{\mathbf{u}}^A\right) - \left(p - p_h, \nabla \cdot E_{\mathbf{u}}^A\right) = 0$$

$$\left(K^{-1}(E_{\mathbf{u}}^I + E_{\mathbf{u}}^A), E_{\mathbf{u}}^A\right) - \left(E_p^I + E_p^A, \nabla \cdot E_{\mathbf{u}}^A\right) = 0$$

$$\left(\mathbf{K}^{-1}E_{\mathbf{u}}^I, E_{\mathbf{u}}^A\right) + \left(\mathbf{K}^{-1}E_{\mathbf{u}}^A, E_{\mathbf{u}}^A\right) - \left(E_p^I, \nabla \cdot E_{\mathbf{u}}^A\right) - \left(E_p^A, \nabla \cdot E_{\mathbf{u}}^A\right) = 0 \quad (4.22)$$

After adding 5.21 and 5.22 we obtain

$$\frac{1}{2}\frac{d}{dt}\left\|E_p^A\right\|^2 + \cancel{\left(\nabla \cdot E_u^A, E_p^A\right)} + \left(\mathbf{K}^{-1}E_{\mathbf{u}}^I, E_{\mathbf{u}}^A\right)$$

$$+ \left(\mathbf{K}^{-1}E_{\mathbf{u}}^A, E_{\mathbf{u}}^A\right) - \left(E_p^I, \nabla \cdot E_{\mathbf{u}}^A\right) - \cancel{\left(E_p^A, \nabla \cdot E_{\mathbf{u}}^A\right)} = 0$$

$$\frac{1}{2}\frac{d}{dt}\left\|E_p^A\right\|^2 + \left(\mathbf{K}^{-1}E_{\mathbf{u}}^I, E_{\mathbf{u}}^A\right) + \left(\mathbf{K}^{-1}E_{\mathbf{u}}^A, E_{\mathbf{u}}^A\right) - \left(E_p^I, \nabla \cdot E_{\mathbf{u}}^A\right) = 0$$

$$\frac{1}{2}\frac{d}{dt}\left\|E_p^A\right\|^2 + \left(\mathbf{K}^{-1}E_{\mathbf{u}}^A, E_{\mathbf{u}}^A\right) = -\left(\mathbf{K}^{-1}E_{\mathbf{u}}^I, E_{\mathbf{u}}^A\right) + \left(E_p^I, \nabla \cdot E_{\mathbf{u}}^A\right)$$

We now take time integral from 0 to T and $E_p^A(0) = \hat{p}(0) - p(0) = 0$.

$$\frac{1}{2}\left\|E_p^A(T)\right\|^2 + \int_0^T \left(\mathbf{K}^{-1}E_{\mathbf{u}}^A, E_{\mathbf{u}}^A\right) d\tau = \underbrace{-\int_0^T \left(\mathbf{K}^{-1}E_{\mathbf{u}}^I, E_{\mathbf{u}}^A\right) d\tau}_{\mathbb{T}_1} + \underbrace{\int_0^T \left(E_p^I, \nabla \cdot E_{\mathbf{u}}^A\right) d\tau}_{\mathbb{T}_2}$$

$$(4.23)$$

The terms from the right hand side can be handled separately.

$$\mathbb{T}_1 = -\int_0^T \left(\mathbf{K}^{-1} E_{\mathbf{u}}^I, E_{\mathbf{u}}^A\right) d\tau \tag{4.24}$$

$$\leq \int_0^T \left\| \mathbf{K}^{-1} E_{\mathbf{u}}^I \right\| \left\| E_{\mathbf{u}}^A \right\| d\tau \qquad by\ 5.18 \tag{4.25}$$

$$\leq \frac{1}{2\varepsilon k_{min}^2} \int_0^T \left\| E_{\mathbf{u}}^I \right\|^2 d\tau + \frac{\varepsilon}{2} \int_0^T \left\| E_{\mathbf{u}}^A \right\|^2 d\tau \tag{4.26}$$

We should note that

$$\left(E_p^I, \nabla \cdot E_{\mathbf{u}}^A\right)_{\Omega} = \left(E_p^I, \nabla \cdot E_{\mathbf{u}}^A\right)_{\Omega^*} + \underbrace{\left(E_p^I, \nabla \cdot E_{\mathbf{u}}^A\right)_{\Omega \setminus \Omega^*}}_{0} = \left(E_p^I, \nabla \cdot E_{\mathbf{u}}^A\right)_{\Omega^*}$$

since $\nabla \cdot E_{\mathbf{u}}^A \Big|_{\Omega \setminus \Omega^*} \in W_h$ and the property 5.13.

$$\mathbb{T}_2 = \int_0^T \left(E_p^I, \nabla \cdot E_{\mathbf{u}}^A\right)_{\Omega} d\tau$$

$$= \int_0^T \left(E_p^I, \nabla \cdot E_{\mathbf{u}}^A\right)_{\Omega^*} d\tau$$

$$\leq \int_0^T \left\| E_p^I \right\|_{\Omega^*} \left\| \nabla \cdot E_{\mathbf{u}}^A \right\|_{\Omega^*} d\tau \underbrace{\leq}_{5.16, 5.19}$$

$$\leq C \int_0^T h \left\| p \right\|_{1, \Omega^*} h^{-1} \left\| E_{\mathbf{u}}^A \right\|_{\Omega^*} d\tau \tag{4.27}$$

$$\leq C \int_0^T \left\| p \right\|_{1, \Omega^*} \left\| E_{\mathbf{u}}^A \right\|_{\Omega} d\tau \qquad by\ 5.18$$

$$\leq \frac{C}{2\varepsilon} \int_0^T \left\| p \right\|_{1, \Omega^*}^2 d\tau + \frac{\varepsilon}{2} \int_0^T \left\| E_{\mathbf{u}}^A \right\|^2 d\tau$$

$$\int_0^T \left(K^{-1} E_{\mathbf{u}}^A, E_{\mathbf{u}}^A\right) d\tau \geq \int_0^T \frac{1}{k_{max}} \left(E_{\mathbf{u}}^A, E_{\mathbf{u}}^A\right) d\tau = \frac{1}{k_{max}} \int_0^T \left\| E_{\mathbf{u}}^A \right\|^2 d\tau \tag{4.28}$$

So by 5.23, 5.24, 5.27, and 5.28 we get

$$\frac{1}{2}\left\|E_p^A(T)\right\|^2 + \frac{1}{k_{max}}\int_0^T \left\|E_{\mathbf{u}}^A\right\|^2 d\tau$$

$$\leq \frac{1}{2}\left\|E_p^A(T)\right\|^2 + \int_0^T \left(\mathbf{K}^{-1}E_{\mathbf{u}}^A, E_{\mathbf{u}}^A\right) d\tau = \mathbb{T}_1 + \mathbb{T}_2$$

$$\leq \frac{1}{2\varepsilon k_{min}^2}\int_0^T \left\|E_{\mathbf{u}}^I\right\|^2 d\tau + \frac{\varepsilon}{2}\int_0^T \left\|E_{\mathbf{u}}^A\right\|^2 d\tau + \frac{C}{2\varepsilon}\int_0^T \|p\|_{1,\Omega^*}^2 d\tau + \frac{\varepsilon}{2}\int_0^T \left\|E_{\mathbf{u}}^A\right\|^2 d\tau$$

$$\frac{1}{2}\left\|E_p^A(T)\right\|^2 + \left(\frac{1}{k_{max}} - \varepsilon\right)\int_0^T \left\|E_{\mathbf{u}}^A\right\|^2 d\tau$$

$$\leq \frac{1}{2\varepsilon k_{min}^2}\int_0^T \left\|E_{\mathbf{u}}^I\right\|^2 d\tau + \frac{C}{2\varepsilon}\int_0^T \|p\|_{1,\Omega^*}^2 d\tau$$

$$\leq \frac{C}{2\varepsilon k_{min}^2}\int_0^T h^2 \|\mathbf{u}\|_1^2 d\tau + \frac{C}{2\varepsilon}\int_0^T h \|p\|_{1,\infty,\Omega^*}^2 d\tau$$

$$\leq C\left(h^2\int_0^T \|\mathbf{u}\|_1^2 d\tau + h\int_0^T \|p\|_{1,\infty,\Omega^*}^2 d\tau\right)$$

where ε and C are independent of T and h. We can make ε small enough in order to have LHS with positive coefficients. Later take minimum and divide both side of inequality. At RHS, we used fact that $|\Omega^*| \leq Ch$.

$$\left\|E_p^A(T)\right\|^2 + \int_0^T \left\|E_{\mathbf{u}}^A\right\|^2 d\tau \leq C\left(h^2\int_0^T \|\mathbf{u}\|_1^2 d\tau + h\int_0^T \|p\|_{1,\infty,\Omega^*}^2 d\tau\right) \tag{4.29}$$

Since $T \geq 0$, and take $\sup_{0\leq\tau\leq T}$

$$\sup_{0\leq\tau\leq T}\left\|E_p^A(\tau)\right\|^2 + \int_0^T \left\|E_{\mathbf{u}}^A\right\|^2 d\tau \leq C\left(h^2\int_0^T \|\mathbf{u}\|_1^2 d\tau + h\int_0^T \|p\|_{1,\infty,\Omega^*}^2 d\tau\right)$$

71

from which the theorem easily follows.

$$\left\| E_p^A \right\|_{L^\infty([0,T];L^2)}^2 + \left\| E_\mathbf{u}^A \right\|_{L^2([0,T];L^2)}^2 \leq C \left(h^2 \int_0^T \|\mathbf{u}\|_1^2 \, d\tau + h \int_0^T \|p\|_{1,\infty,\Omega^*}^2 \, d\tau \right)$$

$\square$

Remark.We used the following lemma after taking sup.

Lemma 4.2.3. *Let $f(\tau) \geq 0$ then*

$$\sup_{0 \leq t \leq T} \int_0^t f(\tau) d\tau = \int_0^T f(\tau) d\tau$$

Proof. Let $F(t) = \int_0^t f(\tau) d\tau$ then $\frac{d}{dt} F(t) = f(t) \geq 0$. F(t) is an increasing function. So $\sup_{0 \leq t \leq T} F(t) = F(T)$. $\square$

Theorem 4.2.4 (Error estimate)**.** *Let's have same conditions as in the previous theorem. Then the following error estimate holds:*

$$\|p - p_h\|_{L^\infty([0,T];L^2)}^2 + \|\mathbf{u} - \mathbf{u}_h\|_{L^2([0,T];L^2)}^2 \leq C(h^2 + h) \qquad (4.30)$$

Proof. By applying triangle inequality,the Interpolation Error Inequalities and

Theorem 5.2.2 results we obtain:

$$\|p - p_h\|_{L^\infty([0,T];L^2)}^2 + \|\mathbf{u} - \mathbf{u}_h\|_{L^2([0,T];L^2)}^2$$

$$= \left\|E_p^I + E_p^A\right\|_{L^\infty([0,T];L^2)}^2 + \left\|E_\mathbf{u}^I + E_\mathbf{u}^A\right\|_{L^2([0,T];L^2)}^2$$

$$\leq C \left(\underbrace{\left\|E_p^I\right\|_{L^\infty([0,T];L^2)}^2 + \left\|E_\mathbf{u}^I\right\|_{L^2([0,T];L^2)}^2}_{Interpolation\ error} + \underbrace{\left\|E_p^A\right\|_{L^\infty([0,T];L^2)}^2 + \left\|E_\mathbf{u}^A\right\|_{L^2([0,T];L^2)}^2}_{Auxiliary\ error} \right)$$

$$\leq C(T, p, \mathbf{u}, K)(h^2 + h)$$

$\square$

4.3 A *priori* error estimation for Parabolic with Enhanced velocity Mixed FEM, the discrete in time case

Let's start with some definitions. Let $\Delta t = \frac{T}{N}$, N is a positive integer, $t_n = n\Delta t$. For given $\theta \in [0, 1]$:

$$f^n = f(x, t_n), \qquad 0 \le n \le N, \tag{4.31}$$

$$f^{n,\theta} = \frac{1}{2}(1+\theta)f^{n+1} + \frac{1}{2}(1-\theta)f^n, \qquad 0 \le n \le N-1. \tag{4.32}$$

For convenience, let's make also the following definitions:

$$\|f\|_{l^\infty(L^2)} = \max_{0 \le n \le N} \|f^n\|_{L^2}$$

$$\|f\|_{l^2(L^p)} = \left(\sum_{n=0}^{N-1} \|f^{n,\theta}\|_{L^p}^2 \, \Delta t \right)^{\frac{1}{2}}$$

A small remark:

$$t^{n,\theta} = \frac{1}{2}(1+\theta)t^{n+1} + \frac{1}{2}(1-\theta)t^n = \frac{1}{2}(1+\theta)t^n + \frac{1}{2}(1+\theta)\Delta t + \frac{1}{2}(1-\theta)t^n =$$

$$= t^n + \frac{1}{2}(1+\theta)\Delta t$$

OR $\qquad t^{n,\theta} - t^n = \frac{1}{2}(1+\theta)\Delta t.$

For any sufficiently smooth function $f(t)$, by using the Taylor series expansion about $t = t^{n,\theta}$, we obtain:

$$f^{n+1} = f\Big|_{t=t^{n,\theta}} + \frac{1}{2}(1-\theta)\Delta t \frac{\partial f}{\partial t}\Big|_{t=t^{n,\theta}} + \frac{1}{8}(1-\theta)^2(\Delta t)^2 \frac{\partial^2 f}{\partial t^2}\Big|_{t=t^{n,\theta}} + O(\Delta t^3)$$

$$f^n = f\Big|_{t=t^{n,\theta}} - \frac{1}{2}(1+\theta)\Delta t \frac{\partial f}{\partial t}\Big|_{t=t^{n,\theta}} + \frac{1}{8}(1+\theta)^2(\Delta t)^2 \frac{\partial^2 f}{\partial t^2}\Big|_{t=t^{n,\theta}} + O(\Delta t^3)$$

Let multiply the first equation by $\frac{1}{2}(1+\theta)$ and the second equation by $\frac{1}{2}(1-\theta)$ and then sum them. We obtain

$$f^{n,\theta} = f\Big|_{t=t^{n,\theta}} + \frac{1}{8}(\Delta t)^2(1+\theta)(1-\theta)\frac{\partial^2 f}{\partial t^2}\Big|_{t=t^{n,\theta}} + O(\Delta t^3)$$

Note that if $\theta = 1$ then $f^{n,\theta} = f\Big|_{t=t^{n,\theta}}$. In addition, we can get second order approximation of Δt, details in [28] : $p(\mathbf{x}, t^{n,\theta}) \approx p^{n,\theta}$ and $u(\mathbf{x}, t^{n,\theta}) \approx u^{n,\theta}$.

$$\frac{p^{n+1} - p^n}{\Delta t} = p_t(x, t^{n,\theta}) + \rho^{p,n,\theta}, \qquad \forall x \in \Omega, \tag{4.33}$$

where $\rho^{p,n,\theta}$ depends on time-derivatives of p and Δt

$$\left\|\rho^{p,n,\theta}\right\| \leq \begin{cases} C_1 \Delta t \left\|p_{tt}\right\|_{L^\infty((t^n,t^{n+1}),H^1)}, & if \quad \theta = 1 \\ C_2 \Delta t^2 \left\|p_{ttt}\right\|_{L^\infty((t^n,t^{n+1}),H^1)}, & if \quad \theta = 0 \end{cases} \tag{4.34}$$

The variational problem: Find $\mathbf{u}_h \in \mathbf{V}_h^*$ and $p_h \in W_h$ such that

$$\left(\frac{\partial p_h}{\partial t}, w\right) + (\nabla \cdot \mathbf{u}_h, w) = l_1(w) \qquad\qquad \forall w \in W_h \tag{4.35}$$

$$\left(\mathbf{K}^{-1}\mathbf{u}_h, \mathbf{v}\right) - (p_h, \nabla \cdot \mathbf{v}) = l_2(\mathbf{v}) \qquad\qquad \forall \mathbf{v} \in \mathbf{V}_h^* \tag{4.36}$$

In addition, there is an initial condition

$$(p_h, w)\Big|_{t=0} = (p_0, w) \qquad\qquad \forall w \in W_h \tag{4.37}$$

75

where l_1 and l_2 are bounded linear functionals, i.e.

$$l_1(w) = (f, w),$$

$$l_2(\mathbf{v}) = -\langle g, \mathbf{v} \cdot \nu \rangle_{\partial\Omega}.$$

With this definitions, Equations 5.35 and 5.36 become:

$$\left(\frac{p_h^{n+1} - p_h^n}{\Delta t}, w\right) + \left(\nabla \cdot \mathbf{u}_h^{n,\theta}, w\right) = l_1^{n,\theta}(w) \qquad \forall w \in W_h \qquad (4.38)$$

$$\left(\mathbf{K}^{-1}\mathbf{u}_h^{n,\theta}, \mathbf{v}\right) - \left(p_h^{n,\theta}, \nabla \cdot \mathbf{v}\right) = l_2^{n,\theta}(\mathbf{v}) \qquad \forall \mathbf{v} \in \mathbf{V}_h^* \qquad (4.39)$$

Note that if $\theta = 1$ then the backward Euler(Implicit) method, and if $\theta = 0$ then the Crank-Nicolson scheme.

Let's consider true solution $(\mathbf{u}, p) \in (\mathbf{V}, W)$ of Equations 5.5 and 5.6 at time $t = t^{n,\theta}$ in the continuous in time with spatially discrete scheme. We used Equation 5.33 and additional remark related to the Taylor series expansion in order to obtain the following equations with at least order of $O(\Delta t)$:

$$\left(\frac{p^{n+1} - p^n}{\Delta t}, w\right) + \left(\nabla \cdot \mathbf{u}^{n,\theta}, w\right) = l_1(w) + \underbrace{\left(\rho^{p,n,\theta}, w\right)}_{O(\Delta t)} \qquad \forall w \in W \quad (4.40)$$

$$\left(K^{-1}\mathbf{u}^{n,\theta}, \mathbf{v}\right) - \left(p^{n,\theta}, \nabla \cdot \mathbf{v}\right) = l_2(\mathbf{v}) \qquad \forall \mathbf{v} \in \mathbf{V} \qquad (4.41)$$

Next, let's subtract Equations $5.40 - 5.41$ from $5.38 - 5.39$ we have :

$$\left(\frac{p^{n+1} - p_h^{n+1} - (p^n - p_h^n)}{\Delta t}, w\right) + \left(\nabla \cdot \left(\mathbf{u}^{n,\theta} - \mathbf{u}_h^{n,\theta}\right), w\right) = \left(\rho^{p,n,\theta}, w\right) \qquad \forall w \in W_h$$

$$(4.42)$$

$$\left(K^{-1}\left(\mathbf{u}^{n,\theta} - \mathbf{u}_h^{n,\theta}\right), \mathbf{v}\right) - \left(p^{n,\theta} - p_h^{n,\theta}, \nabla \cdot \mathbf{v}\right) = 0 \quad \forall \mathbf{v} \in \mathbf{V}_h^* \qquad (4.43)$$

76

Take $\mathbf{v} = \Pi^* \mathbf{u}^{n,\theta} - \mathbf{u}_h^{n,\theta} = E_{\mathbf{u}}^{A\ n,\theta}$ and $w = E_p^{A\ n,\theta}$ in 5.43 and 5.42 respectively.

$$\left(\frac{\left(E_p^{I\ n+1} + E_p^{A\ n+1} \right) - \left(E_p^{I\ n} + E_p^{A\ n} \right)}{\Delta t}, E_p^{I\ n,\theta} \right)$$
$$+ \left(\nabla \cdot \left(E_{\mathbf{u}}^{I\ n,\theta} + E_{\mathbf{u}}^{A\ n,\theta} \right), E_p^{I\ n,\theta} \right) = \left(\rho^{p,n,\theta}, E_p^{A\ n,\theta} \right)$$

$$\left(\mathbf{K}^{-1} \left(E_{\mathbf{u}}^{I\ n,\theta} + E_{\mathbf{u}}^{A\ n,\theta} \right), E_{\mathbf{u}}^{A\ n,\theta} \right) - \left(E_p^{I\ n,\theta} + E_p^{A\ n,\theta}, \nabla \cdot E_{\mathbf{u}}^{A\ n,\theta} \right) = 0$$

Combining them we can rewrite as

$$\left(\frac{\left(E_p^{I\,n+1} + E_p^{A\,n+1} \right) - \left(E_p^{I\,n} + E_p^{A\,n} \right)}{\Delta t}, E_p^{A\,n,\theta} \right) + \left(\nabla \cdot \left(E_{\mathbf{u}}^{I\,n,\theta} + E_{\mathbf{u}}^{A\,n,\theta} \right), E_p^{A\,n,\theta} \right) +$$

$$+ \left(\mathbf{K}^{-1} \left(E_{\mathbf{u}}^{I\,n,\theta} + E_{\mathbf{u}}^{A\,n,\theta} \right), E_{\mathbf{u}}^{A\,n,\theta} \right) - \left(E_p^{I\,n,\theta} + E_p^{A\,n,\theta}, \nabla \cdot E_{\mathbf{u}}^{A\,n,\theta} \right) =$$

$$= \left(\frac{E_p^{I\,n+1} + E_p^{A\,n+1}}{\Delta t}, E_p^{A\,n} \right) - \left(\frac{E_p^{I\,n} + E_p^{A\,n}}{\Delta t}, E_p^{A\,n,\theta} \right)$$

$$+ \left(\nabla \cdot E_{\mathbf{u}}^{I\,n,\theta}, E_p^{A\,n,\theta} \right) + \cancel{\left(\nabla \cdot E_{\mathbf{u}}^{A\,n,\theta}, E_p^{A\,n,\theta} \right)}$$

$$+ \left(\mathbf{K}^{-1} \left(E_{\mathbf{u}}^{I\,n,\theta} + E_{\mathbf{u}}^{A\,n,\theta} \right), E_{\mathbf{u}}^{A\,n,\theta} \right) - \left(E_p^{I\,n,\theta}, \nabla \cdot E_{\mathbf{u}}^{A\,n,\theta} \right) - \cancel{\left(E_p^{A\,n,\theta}, \nabla \cdot E_{\mathbf{u}}^{A\,n,\theta} \right)}$$

$$= \overset{0,\ by\ 5.13}{\cancel{\left(\frac{E_p^{I\,n+1}}{\Delta t}, E_p^{A\,n,\theta} \right)}} \quad + \quad \left(\frac{E_p^{A\,n+1}}{\Delta t}, E_p^{A\,n,\theta} \right)$$

$$- \overset{0,\ by\ 5.13}{\cancel{\left(\frac{E_p^{I\,n}}{\Delta t}, E_p^{A\,n,\theta} \right)}} - \left(\frac{E_p^{A\,n}}{\Delta t}, E_p^{A\,n,\theta} \right) + \overset{0,\ by\ 5.14}{\cancel{\left(\nabla \cdot E_{\mathbf{u}}^{I\,n,\theta}, E_p^{A\,n,\theta} \right)}}$$

$$+ \left(\mathbf{K}^{-1} \left(E_{\mathbf{u}}^{I\,n,\theta} + E_{\mathbf{u}}^{A\,n,\theta} \right), E_{\mathbf{u}}^{A\,n,\theta} \right) - \left(E_p^{I\,n,\theta}, \nabla \cdot E_{\mathbf{u}}^{A\,n,\theta} \right)$$

$$= \left(\frac{E_p^{A\,n+1} - E_p^{A\,n}}{\Delta t}, E_p^{A\,n,\theta} \right) + \left(\mathbf{K}^{-1} \left(E_{\mathbf{u}}^{I\,n,\theta} + E_{\mathbf{u}}^{A\,n,\theta} \right), E_{\mathbf{u}}^{A\,n,\theta} \right) - \left(E_p^{I\,n,\theta}, \nabla \cdot E_{\mathbf{u}}^{A\,n,\theta} \right)$$

$$= \left(\rho^{p,n,\theta}, E_p^{A\,n,\theta} \right)$$

$$\left(\frac{E_p^{A\,n+1} - E_p^{A\,n}}{\Delta t}, E_p^{A\,n,\theta} \right) + \left(\mathbf{K}^{-1} E_{\mathbf{u}}^{A\,n,\theta}, E_{\mathbf{u}}^{A\,n,\theta} \right)$$

$$= -\left(\mathbf{K}^{-1} E_{\mathbf{u}}^{I\,n,\theta}, E_{\mathbf{u}}^{A\,n,\theta} \right) + \left(E_p^{I\,n,\theta}, \nabla \cdot E_{\mathbf{u}}^{A\,n,\theta} \right) + \left(\rho^{p,n,\theta}, E_p^{A\,n,\theta} \right) \tag{4.44}$$

$$\left(\frac{E_p^{A\,n+1} - E_p^{A\,n}}{\Delta t}, E_p^{A\,n,\theta} \right) = \left(\frac{E_p^{A\,n+1} - E_p^{A\,n}}{\Delta t}, \frac{1+\theta}{2} E_p^{A\,n+1,\theta} + \frac{1-\theta}{2} E_p^{A\,n,\theta} \right)$$

$$= \frac{1+\theta}{2\Delta t} \left(E_p^{A\,n+1} - E_p^{A\,n}, E_p^{A\,n+1} \right) + \frac{1-\theta}{2\Delta t} \left(E_p^{A\,n+1} - E_p^{A\,n}, E_p^{A\,n} \right)$$

$$= \frac{1+\theta}{2\Delta t} \left(E_p^{A\,n+1}, E_p^{A\,n+1} \right) - \frac{1+\theta}{2\Delta t} \left(E_p^{A\,n}, E_p^{A\,n+1} \right)$$

$$+ \frac{1-\theta}{2\Delta t} \left(E_p^{A\,n+1}, E_p^{A\,n} \right) - \frac{1-\theta}{2\Delta t} \left(E_p^{A\,n}, E_p^{A\,n} \right)$$

$$= \frac{1+\theta}{2\Delta t} \left\| E_p^{A\,n+1} \right\|^2 - \frac{2\theta}{2\Delta t} \left(E_p^{A\,n}, E_p^{A\,n+1} \right) - \frac{1-\theta}{2\Delta t} \left\| E_p^{A\,n} \right\|^2$$

$$= \frac{1}{2\Delta t} \left\| E_p^{A\,n+1} \right\|^2 - \frac{1}{2\Delta t} \left\| E_p^{A\,n} \right\|^2 + \frac{\theta}{2\Delta t} \left(\left\| E_p^{A\,n+1} \right\|^2 - 2 \left(E_p^{A\,n}, E_p^{A\,n+1} \right) + \left\| E_p^{A\,n} \right\|^2 \right)$$

$$= \frac{1}{2\Delta t} \left(\left\| E_p^{A\,n+1} \right\|^2 - \left\| E_p^{A\,n} \right\|^2 \right) + \underbrace{\frac{\theta}{2\Delta t} \left(\left\| E_p^{A\,n+1} \right\| - \left\| E_p^{A\,n} \right\| \right)^2}_{\geq 0} \geq$$

$$\geq \frac{1}{2\Delta t} \left(\left\| E_p^{A\,n+1} \right\|^2 - \left\| E_p^{A\,n} \right\|^2 \right)$$

It follows immediately that

$$\left(\frac{E_p^{A\,n+1} - E_p^{A\,n}}{\Delta t}, E_p^{A\,n,\theta} \right) \geq \frac{1}{2\Delta t} \left(\left\| E_p^{A\,n+1} \right\|^2 - \left\| E_p^{A\,n} \right\|^2 \right) \tag{4.45}$$

By using 5.45, multiply by $2\Delta t$ and sum from 0 to $N-1$ in Equation 5.44.

$$\sum_{n=0}^{N-1} \left(\left\| E_p^{A\,n+1} \right\|^2 - \left\| E_p^{A\,n} \right\|^2 \right) + \sum_{n=0}^{N-1} \left(\mathbf{K}^{-1} E_{\mathbf{u}}^{A\,n,\theta}, E_{\mathbf{u}}^{A\,n,\theta} \right) \Delta t \leq$$

$$\leq -2 \sum_{n=0}^{N-1} \left(\mathbf{K}^{-1} E_{\mathbf{u}}^{I\,n,\theta}, E_{\mathbf{u}}^{A\,n,\theta} \right) \Delta t + 2 \sum_{n=0}^{N-1} \left(E_p^{I\,n,\theta}, \nabla \cdot E_{\mathbf{u}}^{A\,n,\theta} \right) \Delta t + 2 \sum_{n=0}^{N-1} \left(\rho^{p,n,\theta}, E_p^{A\,n,\theta} \right) \Delta t$$

$$\left(\left\| E_p^{A\,N} \right\|^2 - \overbrace{\left\| E_p^{A\,\theta} \right\|^2}^{} \right)^{\!\!\! 0,\ by\ 5.37} + \sum_{n=0}^{N-1} \left(\mathbf{K}^{-1} E_{\mathbf{u}}^{A\,n,\theta}, E_{\mathbf{u}}^{A\,n,\theta} \right) \Delta t$$

$$\leq \underbrace{-2 \sum_{n=0}^{N-1} \left(\mathbf{K}^{-1} E_{\mathbf{u}}^{I\,n,\theta}, E_{\mathbf{u}}^{A\,n,\theta} \right) \Delta t}_{\mathbb{T}_1} + \underbrace{2 \sum_{n=0}^{N-1} \left(\rho^{p,n,\theta}, E_p^{A\,n,\theta} \right) \Delta t}_{\mathbb{T}_2} + \underbrace{2 \sum_{n=0}^{N-1} \left(E_p^{I\,n,\theta}, \nabla \cdot E_{\mathbf{u}}^{A\,n,\theta} \right) \Delta t}_{\mathbb{T}_3}$$

$$\mathbb{T}_1 = -2 \sum_{n=0}^{N-1} \left(\mathbf{K}^{-1} E_{\mathbf{u}}^{I\,n,\theta}, E_{\mathbf{u}}^{A\,n,\theta} \right) \Delta t$$

$$\underbrace{\leq}_{Holder's\ ineq.} 2 \sum_{n=0}^{N-1} \left\| \mathbf{K}^{-1} E_{\mathbf{u}}^{I\,n,\theta} \right\| \left\| E_{\mathbf{u}}^{A\,n,\theta} \right\| \Delta t$$

$$\underbrace{\leq}_{Young's\ ineq.} \frac{1}{\varepsilon k_{min}^2} \sum_{n=0}^{N-1} \left\| E_{\mathbf{u}}^{I\,n,\theta} \right\|^2 \Delta t + \varepsilon \sum_{n=0}^{N-1} \left\| E_{\mathbf{u}}^{A\,n,\theta} \right\|^2 \Delta t$$

We use the Holder inequality and the Young inequality to get

$$\mathbb{T}_2 = 2\sum_{n=0}^{N-2} \left(\rho^{p,n,\theta}, E_p^{A\,n,\theta}\right) \Delta t + 2\left(\rho^{p,N-1,\theta}, E_p^{A\,N-1,\theta}\right) \Delta t$$

$$\leq 2\sum_{n=0}^{N-2} \left(\rho^{p,n,\theta}, E_p^{A\,n,\theta}\right) \Delta t + 2\left(\rho^{p,N-1,\theta}, \frac{1+\theta}{2}E_p^{A\,N} + \frac{1-\theta}{2}E_p^{A\,N-1}\right) \Delta t$$

$$\leq 2\sum_{n=0}^{N-2} \left(\rho^{p,n,\theta}, E_p^{A\,n,\theta}\right) \Delta t + 2\left(\Delta t\rho^{p,N-1,\theta}, E_p^{A\,N}\right) + 2\left(\Delta t\rho^{p,N-1,\theta}, E_p^{A\,N-1}\right)$$

$$\leq 2\sum_{n=0}^{N-2} \left\|\rho^{p,n,\theta}\right\| \left\|E_p^{A\,n,\theta}\right\| \Delta t + 2\left\|\Delta t\rho^{p,N-1,\theta}\right\| \left\|E_p^{A\,N}\right\| + 2\left\|\Delta t\rho^{p,N-1,\theta}\right\| \left\|E_p^{A\,N-1}\right\|$$

$$\leq 2\left(\sum_{n=0}^{N-2} 8\left\|\rho^{p,n,\theta}\right\|^2 + \frac{1}{8}\sum_{n=0}^{N-2} \left\|E_p^{A\,n,\theta}\right\|^2\right) \Delta t$$

$$+ \frac{1}{2}\left\|E_p^{A\,N}\right\|^2 + C\left\|E_p^{A\,N-1}\right\|^2 + C\left\|\rho^{p,N-1,\theta}\right\| \Delta t^2$$

$$\leq 16\sum_{n=0}^{N-1} \left\|\rho^{p,n,\theta}\right\|^2 \Delta t + \frac{1}{4}\sum_{n=0}^{N-2} \left\|E_p^{A\,n,\theta}\right\|^2 \Delta t$$

$$+ \frac{1}{2}\left\|E_p^{A\,N}\right\|^2 + C\left\|E_p^{A\,N-1}\right\|^2 + C\left\|\rho^{p,N-1,\theta}\right\| \Delta t^2$$

$$\leq C\sum_{n=0}^{N-1} \left\|\rho^{p,n,\theta}\right\|^2 \Delta t + C\sum_{n=0}^{N-1} \left\|E_p^{A\,n}\right\|^2 \Delta t + \frac{1}{2}\left\|E_p^{A\,N}\right\|^2 + C\left\|\rho^{p,N-1,\theta}\right\| \Delta t^2$$

We should note that

$$\left(E_p^I, \nabla \cdot E_u^A\right)_\Omega = \left(E_p^I, \nabla \cdot E_u^A\right)_{\Omega^*} + \underbrace{\left(E_p^I, \nabla \cdot E_u^A\right)_{\Omega\backslash\Omega^*}}_{0} = \left(E_p^I, \nabla \cdot E_u^A\right)_{\Omega^*}$$

$$(4.46)$$

since $\nabla \cdot E_u^A\Big|_{\Omega\backslash\Omega^*} \in W_h$ and the property 5.13.

$$\mathbb{T}_3 = 2 \sum_{n=0}^{N-1} \left(E_p^{I\ n,\theta}, \nabla \cdot E_{\mathbf{u}}^{A\ n,\theta} \right)_\Omega \Delta t$$

$$= 2 \sum_{n=0}^{N-1} \left(E_p^{I\ n,\theta}, \nabla \cdot E_{\mathbf{u}}^{A\ n,\theta} \right)_{\Omega^*} \Delta t$$

$$\leq 2 \sum_{n=0}^{N-1} \left\| E_p^{I\ n,\theta} \right\|_{\Omega^*} \left\| \nabla \cdot E_{\mathbf{u}}^{A\ n,\theta} \right\|_{\Omega^*} \Delta t \leq$$

$$\leq 2C \sum_{n=0}^{N-1} \left(\frac{1+\theta}{2} \left\| p^{n+1} \right\|_{1,\Omega^*} + \frac{1-\theta}{2} \left\| p^n \right\|_{1,\Omega^*} \right) h \left\| E_{\mathbf{u}}^{A\ n,\theta} \right\|_\Omega h^{-1} \Delta t$$

$$\leq C \sum_{n=0}^{N-1} \left(\frac{1+\theta}{2} \left\| p^{n+1} \right\|_{1,\Omega^*} + \frac{1-\theta}{2} \left\| p^n \right\|_{1,\Omega^*} \right)^2 \Delta t + \varepsilon \sum_{n=0}^{N-1} \left\| E_{\mathbf{u}}^{A\ n,\theta} \right\|^2 \Delta t$$

Remark. We used the following properties:

$$\left\| E_p^{I\ n,\theta} \right\|_{\Omega^*} = \left\| \frac{1+\theta}{2} E_p^{I\ n+1} + \frac{1-\theta}{2} E_p^{I\ n} \right\|_{\Omega^*}$$

$$\leq \frac{1+\theta}{2} \left\| E_p^{I\ n+1} \right\|_{\Omega^*} + \frac{1-\theta}{2} \left\| E_p^{I\ n} \right\|_{\Omega^*}$$

$$\leq \frac{1+\theta}{2} \left\| p^{n+1} \right\|_{1,\Omega^*} h + \frac{1-\theta}{2} \left\| p^n \right\|_{1,\Omega^*} h$$

$$\leq \left(\frac{1+\theta}{2} \left\| p^{n+1} \right\|_{1,\Omega^*} + \frac{1-\theta}{2} \left\| p^n \right\|_{1,\Omega^*} \right) h$$

and

$$\left\| \nabla \cdot E_{\mathbf{u}}^{A\ n,\theta} \right\|_{\Omega^*} \leq C \left\| E_{\mathbf{u}}^{A\ n,\theta} \right\|_{\Omega^*} h^{-1} \leq C \left\| E_{\mathbf{u}}^{A\ n,\theta} \right\|_\Omega h^{-1}$$

Next, we know that

$$\left(\mathbf{K}^{-1} E_{\mathbf{u}}^{A\ n,\theta}, E_{\mathbf{u}}^{A\ n,\theta}\right) \geq \frac{1}{k_{max}} \left\| E_{\mathbf{u}}^{A\ n,\theta} \right\|^2$$

Therefore,

$$\frac{1}{2} \left\| E_p^{A\ N} \right\|^2 + \left[\frac{2}{k_{max}} - 2\varepsilon \right] \sum_{n=0}^{N-1} \left\| E_{\mathbf{u}}^{A\ n,\theta} \right\|^2 \Delta t \leq$$

$$\leq C \sum_{n=0}^{N-1} \left\| E_{\mathbf{u}}^{I\ n,\theta} \right\|^2 \Delta t + C \sum_{n=0}^{N-1} \left\| \rho^{p,n,\theta} \right\|^2 \Delta t + C \sum_{n=0}^{N-1} \left\| E_p^{A\ n} \right\|^2 \Delta t +$$

$$+ \frac{1}{2} \left\| E_p^{A\ N} \right\|^2 \Delta t + + C \sum_{n=0}^{N-1} \left(\frac{1+\theta}{2} \left\| p^{n+1} \right\|_{1,\Omega^*} + \frac{1-\theta}{2} \left\| p^n \right\|_{1,\Omega^*} \right)^2 \Delta t$$

We can multiply by 2 and make ε small enough in order to have LHS with positive coefficients. Later take minimum and divide both side of inequality.

$$\sum_{n=0}^{N-1} \left\| E_{\mathbf{u}}^{A\ n,\theta} \right\|^2 \Delta t + \left\| E_p^{A\ N} \right\|^2 \leq$$

$$\leq C\Delta t \left[\sum_{n=0}^{N-1} \left\| E_{\mathbf{u}}^{I\ n,\theta} \right\|^2 + \sum_{n=0}^{N-1} \left(\frac{1+\theta}{2} \left\| p^{n+1} \right\|_{1,\Omega^*} + \frac{1-\theta}{2} \left\| p^n \right\|_{1,\Omega^*} \right)^2 \right]$$

$$+ C \sum_{n=0}^{N-1} \left\| E_p^{A\ n} \right\|^2 \Delta t + C \sum_{n=0}^{N-1} \left\| \rho^{p,n,\theta} \right\|^2 \Delta t$$

Thus, we can apply Gronwall's lemma to obtain:

$$\sum_{n=0}^{N-1} \left\| E_{\mathbf{u}}^{A\ n,\theta} \right\|^2 \Delta t + \left\| E_p^{A\ N} \right\|^2$$

$$\leq C \Delta t \left[\sum_{n=0}^{N-1} \left\| E_{\mathbf{u}}^{I\ n,\theta} \right\|^2 + \sum_{n=0}^{N-1} \left(\frac{1+\theta}{2} \left\| p^{n+1} \right\|_{1,\Omega^*} + \frac{1-\theta}{2} \left\| p^n \right\|_{1,\Omega^*} \right)^2 \right] + C \sum_{n=0}^{N-1} \left\| \rho^{p,n,\theta} \right\|^2 \Delta t$$

$$\leq C \Delta t \left[\sum_{n=0}^{N-1} \left\| E_{\mathbf{u}}^{I\ n,\theta} \right\|^2 + h \sum_{n=0}^{N-1} \left(\frac{1+\theta}{2} \left\| p^{n+1} \right\|_{1,\infty,\Omega^*} + \frac{1-\theta}{2} \left\| p^n \right\|_{1,\infty,\Omega^*} \right)^2 \right] + C \sum_{n=0}^{N-1} \left\| \rho^{p,n,\theta} \right\|^2 \Delta t$$

$$\leq C h^2 \sum_{n=0}^{N-1} \left(\frac{1+\theta}{2} \left\| u^{n+1} \right\|_1 + \frac{1-\theta}{2} \left\| u^n \right\|_1 \right)^2 \Delta t +$$

$$+ C h \sum_{n=0}^{N-1} \left(\frac{1+\theta}{2} \left\| p^{n+1} \right\|_{1,\infty,\Omega^*} + \frac{1-\theta}{2} \left\| p^n \right\|_{1,\infty,\Omega^*} \right)^2 \Delta t + C \sum_{n=0}^{N-1} \left\| \rho^{p,n,\theta} \right\|^2 \Delta t$$

$$\leq C(T, \mathbf{u}, p, \mathbf{K}) \left(h^2 + h + \Delta t^{2r} \right).$$

where

$$r = \begin{cases} 1, & if \quad \theta = 1 \\ 2, & if \quad \theta = 0 \end{cases}$$

We used the fact that $\sum_{n=0}^{N-1} \Delta t g_n \leq CT \sum_{n=0}^{N-1} g_n$, $|\Omega^*| \leq Ch$ and Property 5.34. So we conclude the following theorem

Theorem 4.3.1 (Auxiliary error estimate). *Assume $\Delta t > 0$, $\mathbf{K}$ is uniformly positive definite and sufficient regular true solution. Then,*

$$\left\| E_{\mathbf{u}}^A \right\|_{l^2(L^2)}^2 + \left\| E_p^A \right\|_{l^\infty(L^2)}^2 \leq C \left(h^2 + h + \Delta t^{2r} \right) \qquad (4.47)$$

where $C = C(T, \mathbf{K}, \mathbf{u}, p)$ *and*

$$r = \begin{cases} 1, & if \quad \theta = 1 \\ 2, & if \quad \theta = 0 \end{cases}$$

Theorem 4.3.2 (Error estimate). *Let's have same conditions as in previous theorem. Then,*

$$\|p - p_h\|_{l^\infty(L^2)}^2 + \|\mathbf{u} - \mathbf{u}_h\|_{l^2(L^2)}^2 \le C\left(h^2 + h + \Delta t^{2r}\right) \qquad (4.48)$$

where $C = C(T, \mathbf{K}, \mathbf{u}, p)$ *and*

$$r = \begin{cases} 1, & if \quad \theta = 1 \\ 2, & if \quad \theta = 0 \end{cases}$$

Proof. By applying triangle inequality,the Interpolation Error Inequalities and Theorem 5.3.1 results we obtain:

$$\|p - p_h\|_{l^\infty(L^2)}^2 + \|\mathbf{u} - \mathbf{u}_h\|_{l^2(L^2)}^2 = \left\|E_p^I + E_p^A\right\|_{l^\infty(L^2)}^2 + \left\|E_\mathbf{u}^I + E_\mathbf{u}^A\right\|_{l^2(L^2)}^2 \le$$

$$\le C \left(\underbrace{\left\|E_p^I\right\|_{l^\infty(L^2)}^2 + \left\|E_\mathbf{u}^I\right\|_{l^2(L^2)}^2}_{Interpolation\ error} + \underbrace{\left\|E_p^A\right\|_{l^\infty(L^2)}^2 + \left\|E_\mathbf{u}^A\right\|_{l^2(L^2)}^2}_{Auxiliary\ error} \right) \le$$

$$\le C(T, p, \mathbf{u}, \mathbf{K})(h^2 + h) + O(\Delta t^{2r})$$

$\square$

4.4 Numerical examples

In this section, we conduct numerical experiment to verify the numerical accuracy of parabolic problem solution using EVMFEM in space and the backward Euler in time. Based on our a *priori* error analysis estimates we assume a sufficiently smooth analytical solution. In numerical examples, we set $\Omega = (0,1)^2$, $\mathbf{K}_{i,j} = \delta_{i,j}$ and the domain Ω is divided into four subdomains Ω_i; Ω_1 and Ω_4 have fine grids, Ω_2 and Ω_3 have coarse grids; such mesh discretization is illustrated in Figure 5.1.

4.4.1 Numerical example 1

We use manufactured the known solution

$$p(x,y,t) = tx(1-x)y(1-y)$$

and use it to compute the forcing f, the Dirichlet boundary data g, and the initial data p_0. We carry out several levels of uniform grid refinement in each subdomains. The time step and the element size are almost equal to each other, see Table 5.1. The simulation time interval is $(0; 0.1)$, i.e. $T = 0.1$, and we use the Backward Euler method to integrate with regard to time with uniform time step. We are interested in finding the exact error using a given true solution, so the pressure is true error and the velocity error is normalized error. On applying sufficient Newton iterations at each time step provided the residual is within the machine-precision tolerance, we obtain the numerical solution for evaluating of the error in specified norm. We compute $error_p$,

corresponds to $\|p - p_h\|_{l^\infty(L^2)}$, which is maximum of values among time steps that resulting for given time step a discrete pressure L^2-norm that associates only the function values at the cell-centers in space. Also, $error_u$ is defined as $\|\mathbf{u} - \mathbf{u}_h\|_{l^2(L^2)}$ where in space a discrete L^2-norm that associates only the normal vector components at the midpoint edges and then normalized by $\|\mathbf{u}\|_{L^2}$ and l^2-norm in time.
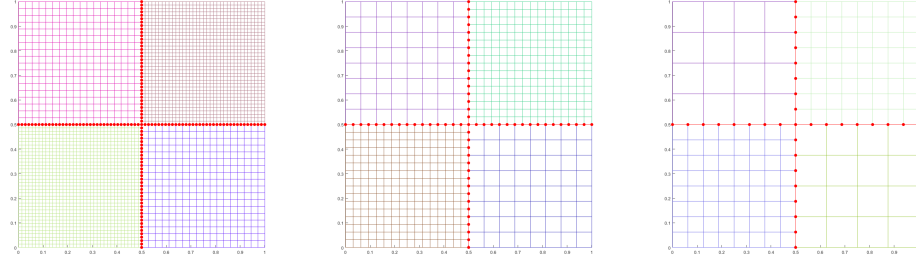

Figure 4.1: Example of non-matching grids for subdomains.

Level	h	H	Δt	$error_p$	$error_u$
1	1/52	1/26	1/50	6.33e-04	1.51e-01
2	1/100	1/50	1/100	3.32e-04	1.02e-01
3	1/120	1/60	1/120	2.79e-04	9.15e-02
4	1/152	1/76	1/150	2.26e-04	7.97e-02

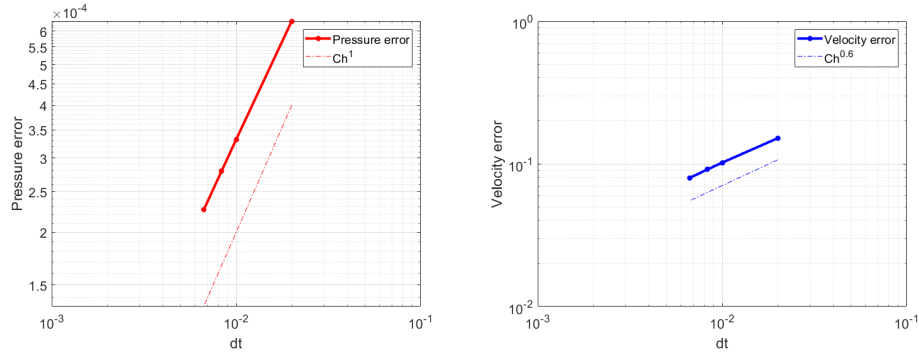Table 4.1: Accuracy results of pressure and velocity for various levels.

Figure 4.2: Convergence of the pressure error and the velocity error.

87

4.4.2 Numerical example 2

We use manufactured the known solution

$$p(x, y, t) = e^t \sin(2\pi x) \sin(2\pi y)$$

and use it to compute the forcing f, the Dirichlet boundary data g, and the initial data p_0. The time step is equal to the root of the coarse mesh size. Thus first order convergence is expected from theoretical result. Such mesh discretization are depicted in the Figure 5.1. The simulation time interval is $(0; 2)$, i.e. $T = 2$, and we use the Backward Euler method to integrate with regard to time with uniform time step, see Table 5.2.

Level	h	H	Δt	$error_p$	$error_u$
1	1/100	1/50	1/7	7.28e-01	8.64e-01
2	1/128	1/64	1/8	6.38e-01	7.71e-01
3	1/164	1/82	1/9	5.69e-01	6.87e-01
4	1/200	1/100	1/10	5.13e-01	6.24e-01

Table 4.2: Accuracy results of pressure and velocity for various levels.
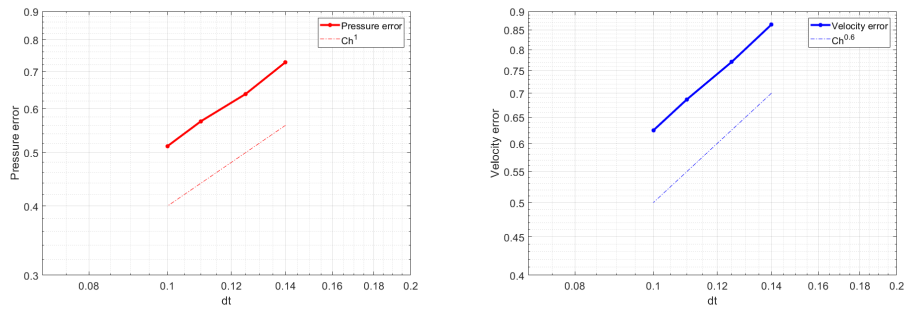

Figure 4.3: Convergence of the pressure error and velocity error.

Bibliography

[1] Aarnes, J. E. and Efendiev, Y. (2006). An adaptive multiscale method for simulation of fluid flow in heterogeneous porous media. *Multiscale Modeling & Simulation*, 5(3):918–939.

[2] Allaire, G. (1989). Homogenization of the Stokes flow in a connected porous medium. *Asymptotic Analysis*, 2(3):203–222.

[3] Allaire, G. (1992). Homogenization and two-scale convergence. *SIAM Journal on Mathematical Analysis*, 23(6):1482–1518.

[4] Amaziane, B., Bourgeat, A., and Jurak, M. (2006). Effective macrodiffusion in solute transport through heterogeneous porous media. *Multiscale Modeling & Simulation*, 5(1):184–204.

[5] Arbogast, T. (2002). Implementation of a locally conservative numerical subgrid upscaling scheme for two-phase darcy flow. *Computational Geosciences*, 6(3-4):453–481.

[6] Arbogast, T. (2012). Mixed multiscale methods for heterogeneous elliptic problems. *Numerical analysis of multiscale problems*, pages 243–283.

[7] Arbogast, T., Cowsar, L. C., Wheeler, M. F., and Yotov, I. (2000). Mixed finite element methods on nonmatching multiblock grids. *SIAM Journal on Numerical Analysis*, 37(4):1295–1315.

[8] Arbogast, T., Minkoff, S. E., and Keenan, P. T. (1998). *An operator-based approach to upscaling the pressure equation*, volume 23. WIT Press.

[9] Arbogast, T., Pencheva, G., Wheeler, M. F., and Yotov, I. (2007). A multiscale mortar mixed finite element method. *Multiscale Modeling & Simulation*, 6(1):319–346.

[10] Arbogast, T., Tao, Z., and Xiao, H. (2013). Multiscale mortar mixed methods for heterogeneous elliptic problems. *Contemp. Math*, 586:9–21.

[11] Arbogast, T. and Wheeler, M. F. (1996). A nonlinear mixed finite element method for a degenerate parabolic equation arising in flow in porous media. *SIAM Journal on Numerical Analysis*, 33(4):1669–1687.

[12] Bensoussan, A., Lions, J.-L., and Papanicolaou, G. (1978). *Asymptotic analysis for periodic structures*, volume 5. North-Holland Publishing Company Amsterdam.

[13] Chung, E., Efendiev, Y., and Hou, T. Y. (2016). Adaptive multiscale model reduction with generalized multiscale finite element methods. *Journal of Computational Physics*, 320:69–95.

[14] De Veubeke, B. F. (1965). Displacement and equilibrium models in the finite element method. *Stress analysis*, 9:145–197.

[15] Durlofsky, L. J. (2003). Upscaling of geocellular models for reservoir flow simulation: a review of recent progress. In *7th International Forum on Reservoir Simulation Bühl/Baden-Baden, Germany*, pages 23–27.

[16] Farmer, C. (2002). Upscaling: A review. *International Journal for Numerical Methods in Fluids*, 40(1-2):63–78.

[17] Ganis, B., Kumar, K., Pencheva, G., Wheeler, M. F., and Yotov, I. (2014). A global jacobian method for mortar discretizations of a fully implicit two-phase flow model. *Multiscale Modeling & Simulation*, 12(4):1401–1423.

[18] Gilbarg, D. and Trudinger, N. S. (2015). *Elliptic partial differential equations of second order*. springer.

[19] Glowinski, R. and Wheeler, M. F. (1988). Domain decomposition and mixed finite element methods for elliptic problems. In *First international symposium on domain decomposition methods for partial differential equations*, pages 144–172.

[20] Hellan, K. (1967). Analysis of elastic plates in flexure by a simplified finite element method. *Acta Polytechnica Scandinavica - Civil Engineering and Building Construction Series*, (46):1.

[21] Hovorka, S. D., Sakurai, S., Kharaka, Y. K., Nance, H. S., Doughty, C., Benson, S. M., Freifeld, B. M., Trautz, R. C., Phelps, T., and Daley, T. M. (2006). Monitoring co2 storage in brine formations: lessons learned from the frio field test one year post injection. *Gulf coast carbon center publication library, Bookshelf*.

[22] Jikov, V. V., Kozlov, S. M., and Oleinik, O. A. (2012). *Homogenization of*

differential operators and integral functionals. Springer Science & Business Media.

[23] Larson, M. G. and Målqvist, A. (2008). A posteriori error estimates for mixed finite element approximations of elliptic problems. *Numerische Mathematik*, 108(3):487–500.

[24] Mikelić, A. (1991). Homogenization of nonstationary Navier-Stokes equations in a domain with a grained boundary. *Annali di Matematica pura ed applicata*, 158(1):167–179.

[25] Mikelić, A., Devigne, V., and Van Duijn, C. (2006). Rigorous upscaling of the reactive flow through a pore, under dominant peclet and damkohler numbers. *SIAM Journal on Mathematical Analysis*, 38(4):1262–1287.

[26] Pavliotis, G. A. and Stuart, A. (2008). *Multiscale methods: averaging and homogenization.* Springer Science & Business Media.

[27] Pencheva, G. V., Vohralík, M., Wheeler, M. F., and Wildey, T. (2013). Robust a posteriori error control and adaptivity for multiscale, multinumerics, and mortar coupling. *SIAM Journal on Numerical Analysis*, 51(1):526–554.

[28] Rivière, B. and Wheeler, M. F. (2000). A discontinuous galerkin method applied to nonlinear parabolic equations. In *Discontinuous Galerkin methods*, pages 231–244. Springer.

[29] Russell, T. F. and Wheeler, M. F. (1983). *Finite element and finite difference methods for continuous flows in porous media*, pages 35–106. SIAM.

[30] Scovazzi, G. (2004). *Multiscale methods in science and engineering*. PhD thesis, stanford university.

[31] Singh, G. and Wheeler, M. F. (2016). Compositional flow modeling using a multi-point flux mixed finite element method. *Computational Geosciences*, 20(3):421–435.

[32] Sun, S. and Wheeler, M. F. (2007). Discontinuous galerkin methods for simulating bioreactive transport of viruses in porous media. *Advances in water resources*, 30(6):1696–1710.

[33] Thomas, S. G. and Wheeler, M. F. (2011). Enhanced velocity mixed finite element methods for modeling coupled flow and transport on non-matching multiblock grids. *Computational Geosciences*, 15(4):605–625.

[34] Tzimas, E., Georgakaki, A., Cortes, C. G., and Peteves, S. (2005). Enhanced oil recovery using carbon dioxide in the european energy system. *Report EUR*, 21895(6).

[35] Vohralík, M. (2010). Unified primal formulation-based a priori and a posteriori error analysis of mixed finite element methods. *Mathematics of Computation*, 79(272):2001–2032.

[36] Weiser, A. and Wheeler, M. F. (1988). On convergence of block-centered finite differences for elliptic problems. *SIAM Journal on Numerical Analysis*, 25(2):351–375.

[37] Wheeler, J. A., Wheeler, M. F., and Yotov, I. (2002). Enhanced velocity mixed finite element methods for flow in multiblock domains. *Computational Geosciences*, 6(3-4):315–332.

[38] Wu, X.-H., Efendiev, Y., and Hou, T. Y. (2002). Analysis of upscaling absolute permeability. *Discrete and Continuous Dynamical Systems Series B*, 2(2):185–204.